TFAW survey II: six newly validated planets and 13 planet candidates from *K2*

D. del Ser [1,2]★ O. Fors [2] M. del Alcázar,[1,2] V. Dyachenko,[3] E. P. Horch,[4] A. Tokovinin [5] C. Ziegler,[6] G. T. van Belle,[7] C. A. Clark[7,8] and Z. D. Hartman[9]

[1]*Observatori Fabra, Reial Acadèmia de Ciències i Arts de Barcelona, Rambla dels Estudis, 115, E-08002 Barcelona, Spain*
[2]*Dept. de Física Quàntica i Astrofísica, Institut de Ciències del Cosmos (ICCUB), Universitat de Barcelona, IEEC-UB, Martí i Franquès 1, E-08028 Barcelona, Spain*
[3]*Special Astrophysical Observatory, 369167 Nizhnij Arkhyz, Russia*
[4]*Department of Physics, Southern Connecticut State University, 501 Crescent Street, New Haven, CT 06515, USA*
[5]*Cerro Tololo Inter-American Observatory, NSF's NOIRLab, Casilla 603, La Serena, Chile*
[6]*Department of Physics, Engineering and Astronomy, Stephen F. Austin State University, TX 75962, USA*
[7]*Lowell Observatory, 1400 W. Mars Hill Road, Flagstaff, AZ 86001, USA*
[8]*Northern Arizona University, 527 S. Beaver Street, Flagstaff, AZ 86011, USA*
[9]*Gemini Observatory/NSF's NOIRLab, 670 N. A'ohoku Place, Hilo, HI, 96720, USA*

ABSTRACT

Searching for Earth-sized planets in data from Kepler's extended mission (*K2*) is a niche that still remains to be fully exploited. The TFAW survey is an ongoing project that aims to re-analyse all light curves in *K2* C1–C8 and C12–C18 campaigns with a wavelet-based detrending and denoising method, and the period search algorithm TLS to search for new transit candidates not detected in previous works. We have analysed a first subset of 24 candidate planetary systems around relatively faint host stars ($10.9 < K_{\rm p} < 15.4$) to allow for follow-up speckle imaging observations. Using vespa and TRICERATOPS, we statistically validate six candidates orbiting four unique host stars by obtaining false-positive probabilities smaller than 1 per cent with both methods. We also present 13 vetted planet candidates that might benefit from other, more precise follow-up observations. All of these planets are sub-Neptune-sized with two validated planets and three candidates with sub-Earth sizes, and have orbital periods between 0.81 and 23.98 d. Some interesting systems include two ultra-short-period planets, three multiplanetary systems, three sub-Neptunes that appear to be within the small planet Radius Gap, and two validated and one candidate sub-Earths (EPIC 210706310.01, K2-411 b, and K2-413 b) orbiting metal-poor stars.

Key words: instrumentation: high angular resolution – methods: data analysis – techniques: photometric – planets and satellites: general – planets and satellites: terrestrial planets.

1 INTRODUCTION

The *K2* mission (Howell et al. 2014) represented a way to continue *Kepler*'s observations after the failure of the spacecraft reaction wheels. This mode, which became fully operational in May 2014, led to a series of 19 sequential campaigns each of which observed a set of independent target fields distributed along the ecliptic plane during ∼80 d.

Given the degraded photometric precision of the *K2* light curves compared to those from the original *Kepler* one, improvements in the data analysis have played a key role in increasing the number of detected planet candidates in *K2* light curves. The first example was the series of pixel decorrelation and detrending algorithms (Vanderburg & Johnson 2014; Deming et al. 2015; Lund et al. 2015) which culminated in the EVEREST 2.0 pipeline (Luger et al. 2018). These have provided the best photometric precision for *K2* light curves and can return photometric precisions very

similar to the ones from the original *Kepler* mission to $K_{\rm p} = 15$ mag. Most planet searches in *K2* campaigns used these EVEREST 2.0-corrected light curves (Mayo et al. 2018; Zink et al. 2020; Adams et al. 2021; Castro-González et al. 2021; de Leon et al. 2021; Zink et al. 2021; Christiansen et al. 2022) and other detrending methods (Kovacs 2020), yielding an appreciable fraction of the currently confirmed planets and candidates. The development of new transit search tools have also helped to increase the number of planets detected. For example, Heller, Hippke & Rodenbeck (2019) was especially sensitive to Earth-sized planets, thanks to the use of the transit least-squares (TLS) algorithm (Hippke & Heller 2019) as a new transit detection tool, which was designed and optimized to detect smaller planets. The definition of robust vetting and statistical validation procedures (Morton 2012, 2015a; Heller et al. 2019; Kruse et al. 2019; Giacalone & Dressing 2020; Giacalone et al. 2021) have also allowed to improve the characterization of false-positive signals originating from background stars, non-associated blended eclipsing binaries, or non-associated stars with transiting planets. All this has led to the admirable current *K2* mission legacy of 537 confirmed planets exclusively

discovered from *K2* observations, and 969 candidates yet to be confirmed.

The current goal of the TFAW survey (del Ser, Fors & Núñez 2018) is to search for new exoplanet candidates previously missed by former studies by further improving the photometric precision of the EVEREST 2.0-corrected light curves. The survey makes use of TFAW, a novel wavelet-based detrending and denoising algorithm developed by del Ser et al. (2018), the EVEREST 2.0 (Luger et al. 2018) processed *K2* light curves, and the TLS (Hippke & Heller 2019) transit search algorithm. As shown in del Ser & Fors (2020), TFAW delivers both better photometric precision and planet characterization than any detrending method applied to *K2* light curves. The increased photometric precision achieved with TFAW, especially for faint *K2* magnitudes, together with TLS improved capabilities to detect small planets, enable us to detect new, Earth-sized, and smaller planets orbiting G-, K-, and M-type stars. As an example of this, del Ser & Fors (2020) reported the discovery of two new statistically validated Earth-sized planets, K2-327 b, and K2-328 b, orbiting an M-type and a K-type star, respectively.

In this work, we present a first sample of 27 new planetary candidates detected by the TFAW survey with new speckle imaging follow-up observations. In Section 2, we describe the observations and ancillary data used in this work, consisting of *K2* EVEREST 2.0-corrected light curves, stellar host characterization, archival high-resolution images, speckle imaging follow-up observations, and *Gaia* eDR3 (Gaia Collaboration 2021) photometry and astrometry. In Section 3, we briefly describe the TFAW algorithm and the transit search method, we present our vetting method, the MCMC-based transit modelling, the mass-radius estimation, and resonance analysis our validation approach, and the candidate disposition procedure. In Section 4, we present and characterize our final validated, candidate, and false-positive sample, and discuss some of the most interesting systems found in this work.

2 DATA AND OBSERVATIONS

2.1 *K2* photometry

The TFAW survey focuses on *K2* campaigns C1–C8, and C12–C18. We exclude campaigns C9, used to study gravitational microlensing events, and C10 and C11, which were separated into subcampaigns. We download ~300 000 EVEREST 2.0 long cadence target light curves recorded before 2019 January 4 available at the MAST archive.[1] Given the characteristics of the wavelet transform used by TFAW (for more details on the algorithm see del Ser et al. 2018; del Ser & Fors 2020) for campaigns C1–C8, we use 3072 epochs while, for campaigns C12–C18, we use 2432. Also, TFAW was designed as a general detrending and denoising tool, and not specifically to analyse *K2* data. To deal with intrapixel and interpixel variations, we use the pixel level decorrelation (PLD) (Deming et al. 2015), and single co-trending basis vector (CBV) corrected fluxes provided by the EVEREST 2.0 pipeline. We also retrieve the available *K2* target pixel files (TPF) and the EVEREST 2.0 photometric apertures of each target. While most of the 27 systems presented in this work were observed in a single *K2* campaign, three (EPIC 211436876, EPIC 246078343, and EPIC 246220667) were observed in two separate campaigns.

The *K2* targets studied in this work together with their corresponding observing campaigns are listed in Table 1.

[1] https://archive.stsci.edu/hlsps/everest/v2/bundles/

Table 1. Summary of the *K2* targets and campaigns, and speckle imaging follow-up facilities used in this work.

EPIC	Campaign	BTA	SOAR	LDT
205979483	3	–	x	–
206461841	3	–	x	–
210418253	4	x	–	–
210706310	4	x	–	–
210708830	4	x	–	–
210768568	4	x	x	–
210945680	4	x	–	–
210967369	4	–	x	–
211436876	5/18	x	–	–
218701083	7	–	x	–
220356827	8	x	x	x
220471100	8	x	–	–
246022853	12	–	x	–
246048459	12	–	x	–
246078343	12/19	–	–	x
246163416	12	–	x	–
246220667	12/19	–	–	x
247223703	13	x	–	–
247422570	13	x	–	–
247560727	13	x	–	–
247744801	13	x	–	–
247874191	13	x	–	–
211572480	18	x	–	–
211705502	18	x	–	–

2.2 Stellar characterization

Robust stellar parameters are critical to ensure unbiased planetary characterization. When available, we update the EPIC catalogue data (Huber, Bryson & et al. 2017) setting the host stellar parameters of our targets to the ones derived by Hardegree-Ullman et al. (2020). They were obtained using a combination of Pan-STARRS DR2 photometry (Flewelling et al. 2020), *Gaia* data, and spectroscopic parameters from the Large Sky Area Multi-Object Fibre Spectroscopic Telescope (LAMOST, Cui et al. 2012) DR5 spectra. de Leon et al. (2021) find that these parameters and the ones obtained with the isochrones package (Morton 2015b) using 2MASS (Skrutskie et al. 2006) photometry and *Gaia* parallaxes and extinctions are in good agreement within $1 - \sigma$. For seven of our targets, we also compare their listed stellar parameters with the ones from the GALAH + DR3 K2-HERMES survey (Buder et al. 2021). For all of them, except for the metallicities of EPIC 206461841, EPIC 210706310, and EPIC 210967369, the K2-HERMES parameters are in good agreement with the Hardegree-Ullman et al. (2020) ones. For EPIC 206461841 and EPIC 210768568, for which there are no derived Hardegree-Ullman et al. (2020) stellar parameters, we use the most recent values from the TESS Input Catalog (TIC) version 8.2 (Paegert et al. 2021). In the case of EPIC 211572480 and EPIC 211705502 (see full discussion in Section 4.5), where, neither Hardegree-Ullman et al. (2020) or EPIC data is available, we do not report stellar information given the astrometry from *Gaia* (see Section 2.5). The stellar limb darkening coefficients are obtained from the tabulated values in Claret (2018), using the available T_{eff}, log *g*, and [Fe/H]. Distances to our candidate host stars are obtained from *Gaia* data (Bailer-Jones et al. 2021). A summary of the stellar parameters of our targets is listed in Table 2.

2.3 Speckle imaging

High-angular resolution imaging of our targets has been made using speckle instruments at three telescopes as listed in Table 1.

Table 2. Summary of stellar parameters. (a) astrometric goodness of fit; (b) astrometric excess noise significance; (c) Renormalized Unit Weight Error.

EPIC	R_s [$R_\odot$]	M_s [$M_\odot$]	T_{eff} [K]	log g [cgs]	[Fe/H] [dex]	K_p [mag]	GOF_AL[a]	D[b]	RUWE[c]	d [pc]	pm [mas yr^{-1}]	notes
205979483	$0.814^{+0.054}_{-0.051}$	$0.945^{+0.425}_{-0.288}$	5414 ± 138	$4.595^{+0.150}_{-0.150}$	-0.028 ± 0.235	12.77	7.19	15.1	1.41	278.08	3.57	★§;
206461841	0.746 ± 0.047	0.800 ± 0.093	4893 ± 119	4.596 ± 0.090	$0.040 \pm 0.048**$	10.89	2.10	24.1	1.11	100.19	118.51	†
210418253	$1.129^{+0.073}_{-0.067}$	$1.325^{+0.590}_{-0.411}$	5296 ± 138	$4.455^{+0.150}_{-0.150}$	0.110 ± 0.235	12.15	1.41	5.86	1.06	217.98	34.07	
210706310	$0.954^{+0.055}_{-0.052}$	$0.709^{+0.304}_{-0.219}$	5941 ± 138	$4.328^{+0.150}_{-0.150}$	$-0.252 \pm 0.081**$	12.29	1.33	7.07	1.05	274.92	62.46	
210708830	$0.760^{+0.018}_{-0.018}$	$1.067^{+0.203}_{-0.173}$	5342 ± 45	$4.704^{0.074}_{-0.074}$	0.015 ± 0.043	13.26	1.35	0.62	1.05	261.71	3.78	
210768568	1.375 ± 0.068	1.018 ± 0.131	5711 ± 105	4.1693 ± 0.074	0.1415 ± 0.0152	11.94	2.66	14.1	1.09	295.87	62.34	†
210945680	$1.059^{+0.018}_{-0.017}$	$0.994^{+0.082}_{-0.075}$	5969 ± 20	$4.386^{+0.031}_{-0.031}$	0.115 ± 0.017	11.32	-0.14	19.6	0.99	226.52	24.37	
210967369	$0.953^{+0.058}_{-0.055}$	$0.845^{+0.372}_{-0.252}$	5534 ± 138	$4.411^{+0.150}_{-0.150}$	$0.320 \pm 0.071**$	12.40	5.44	0.08	1.28	266.98	29.01	
211436876	$1.057^{+0.022}_{-0.020}$	$0.992^{+0.068}_{-0.063}$	5992 ± 14	$4.386^{+0.023}_{-0.023}$	-0.095 ± 0.012	12.30	-2.72	2.36	0.88	370.04	14.73	
218701083	$1.476^{+0.093}_{-0.086}$	$1.198^{+0.521}_{-0.359}$	6262 ± 138	$4.178^{+0.150}_{-0.150}$	-0.184 ± 0.235	12.49	-1.43	0.85	0.93	544.18	8.99	
220356827	$1.270^{+0.086}_{-0.084}$	$0.982^{+0.437}_{-0.298}$	5986 ± 138	$4.222^{+0.150}_{-0.150}$	0.030 ± 0.235	12.58	-0.84	2.68	0.97	504.52	1.95	
220471100	$0.960^{+0.035}_{-0.035}$	$1.365^{+0.234}_{-0.197}$	5197 ± 37	$4.609^{+0.061}_{-0.061}$	0.108 ± 0.035	14.21	21.02	21.1	1.83	547.04	21.99	§;
246022853	$1.114^{+0.162}_{-0.141}$	$0.883^{+0.470}_{-0.315}$	5909 ± 138	$4.287^{+0.150}_{-0.150}$	-0.147 ± 0.235	11.48	32.43	297	3.12	466.31	30.48	★§;
246048459	$0.645^{+0.047}_{-0.044}$	$0.769^{+0.341}_{-0.239}$	4514 ± 138	$4.703^{+0.150}_{-0.150}$	-0.368 ± 0.235	11.60	5.22	0.00	1.07	83.97	14.66	
246078343	$0.700^{+0.055}_{-0.048}$	$0.808^{+0.364}_{-0.256}$	4116 ± 138	$4.656^{+0.150}_{-0.150}$	-0.205 ± 0.235	14.57	2.92	0.97	1.16	292.52	3.37	
246163416	$0.515^{+0.026}_{-0.025}$	$0.512^{+0.058}_{-0.055}$	3734 ± 138	$4.724^{+0.062}_{-0.068}$	-0.101 ± 0.235	13.48	24.62	131	2.44	85.52	199.01	★§;
246220667	$0.732^{+0.055}_{-0.052}$	$0.814^{+0.363}_{-0.251}$	4343 ± 138	$4.621^{+0.150}_{-0.150}$	-0.102 ± 0.235	13.96	0.29	0.00	1.01	255.88	3.86	
247223703	$0.741^{+0.056}_{-0.051}$	$0.861^{+0.394}_{-0.264}$	4434 ± 138	$4.631^{+0.150}_{-0.150}$	-0.087 ± 0.235	14.28	1.90	1.07	1.07	257.94	31.16	
247422570	$0.977^{+0.066}_{-0.063}$	$0.893^{+0.406}_{-0.275}$	5590 ± 138	$4.412^{+0.150}_{-0.150}$	0.014 ± 0.235	15.11	1.21	0.00	1.05	668.62	1.46	
247560727	$0.779^{+0.059}_{-0.054}$	$0.693^{+0.301}_{-0.212}$	5634 ± 138	$4.494^{+0.150}_{-0.150}$	-0.130 ± 0.235	15.43	-0.83	0.00	0.96	680.62	4.92	
247744801	$0.975^{+0.065}_{-0.059}$	$1.027^{+0.451}_{-0.317}$	5214 ± 138	$4.466^{+0.150}_{-0.150}$	0.028 ± 0.235	13.83	-0.71	0.00	0.97	368.81	36.72	
247874191	$1.290^{+0.085}_{-0.080}$	$1.053^{+0.468}_{-0.315}$	5998 ± 138	$4.241^{+0.150}_{-0.150}$	-0.163 ± 0.235	14.54	0.67	0.00	1.02	865.32	4.67	
211572480	–	–	–	–	–	14.10	174.37	1530	12.25	499.84	8.33	★§;
211705502	–	–	–	–	–	13.21	30.94	57.8	2.42	774.16	6.02	§;

Note. ∗: detected companion in Speckle data; §: probable binary from *Gaia* data; †: data from TIC catalogue (Paegert et al. 2021); ∗∗: [Fe/H] from GALAH + DR3 survey (Buder et al. 2021).

The speckle observations at the 6-m Large Alt-Azimuthal Telescope (BTA) of the Special Astrophysical Observatory of the Russian Academy of Sciences (SAO RAS) were obtained in October and December 2021, using its digital speckle interferometer based on EMCCD detectors (Maksimov et al. 2009). 10 of our targets were observed using the 550/20, 700/50, and 800/100 nm filters, three with the 550/20 and 700/50 nm ones, and one target using only the 550/20 mm filter. Most (73 per cent) of the observations were done under good weather conditions, while the remaining ones were done under low-SNR conditions. The calibration methods for the speckle images are listed in Mitrofanova et al. (2020). Positional parameters and magnitude differences were determined using the method described in Balega et al. (2002) and Pluzhnik (2005). One companion was detected at subarcsecond separation (see Table 8).

The 4.3-m Lowell Discovery Telescope (LDT) speckle observations were obtained in August and September of 2021, using the Quad-camera Wavefront-sensing Six-channel Speckle Interferometer (QWSSI) (Clark et al. 2020). Depending on brightness, one thousand to several thousand speckle frames were taken and subsequently analysed according to methods detailed in e.g. Horch et al. (2015). None of the Lowell observations revealed companions, so detection limit curves were constructed from the reconstructed images in each case. These were used to rule out stellar companions with separations and magnitudes that would have been detectable by QWSSI. For these observations, only four of the six wavelength channels were available for use, and of those, the reconstructed images with the highest signal to noise were those taken at 880 nm. Thus, only these were used for the final detection limit curves.

Nineteen EPIC targets from this programme have been observed by the high-resolution speckle camera at the 4.1-m Southern Astrophysical Research Telescope (SOAR) in Chile. The instrument and data processing are described in Tokovinin (2018). The observations were carried out in October–November 2021 (2021.75–2021.80) in the *I* filter (880/140 nm) using the UNC partner time. Three companions at subarcsecond separations were detected (see Table 8). The resolution

limits were from 0.07 to 0.1 arcsec and the typical contrast limit at 1 arcsec separation was around 4 mag.

2.4 Archival imaging

Following a similar approach as the one in de Leon et al. (2021), we downloaded Palomar Observatory Sky Survey (POSS-I) images taken in the 1950s from the Space Telescope Science Institute (STScI) Digitized Survey (DSS)[2] for our targets and compare them to Pan-STARRS DR2[3] (taken between 2012 and 2014) cut-outs, and with the *K2* TPFs. We do this to study the possibility of a chance alignment of our targets with a foreground or background star; especially in the cases of stars with relatively high-proper motions (≥ 50 mas yr^{-1}) or with low-galactic latitudes (as is the case for targets in campaigns C7 and C13).

2.5 *Gaia* eDR3 photometry and astrometry

We use *Gaia* eDR3 to search for neighbouring stars close to our targets. We do this to minimize the chances of biasing our planetary candidates' characterization due to the presence of unresolved stars within the EVEREST 2.0 photometric aperture (Evans, Southworth & Smalley 2016). Resolved *Gaia* detections are plotted in our *K2* TPF validation images (see Fig. 14) and checked during our vetting and validation procedure (see Sections 3.2 and 3.6). We also check for indirect evidence of potential contamination from unresolved stars using the available *Gaia* data for our targets. First, we use *Gaia* astrometric goodness of fit of the astrometric solution for the source in the along-scan direction (GOF_AL) and the astrometric excess noise significance (D) to determine which of our targets could be poorly-resolved binaries (Evans 2018; Gandhi et al. 2022). Evans

[2] https://archive.stsci.edu/cgi-bin/dss_form
[3] https://ps1images.stsci.edu/cgi-bin/ps1cutouts

(2018) manually set `D > 5` and `GOF_AL > 20` to match the boundary between confirmed binaries and confirmed singles. Given that no star in our candidate sample is too bright or has a very high-proper motion, we do not expect any large offset of these parameters to be related to difficulties in modelling saturated or fast-moving stars. Additionally, we use the renormalised unit weight error (RUWE), provided by *Gaia* eDR3 as an extra parameter to identify binary systems from astrometric deviations (Penoyre, Belokurov & Evans 2022). *Gaia* sources with RUWE values significantly greater than one (i.e. significant deviations from the single-body model fit) can be candidate binary systems. We use a rather restrictive value of RUWE > 1.4 as our threshold to determine which of our targets might be unresolved binaries. We choose this value from our analysis of EPIC 205979483 (see Section 2.3) which has `D = 15.1`, `GOF_AL = 7.19`, and `RUWE = 1.41`. Although, `GOF_AL` is smaller than its proposed threshold value, `D` exceeds it. In addition, we also detect a very faint object separated 0.5751 arcsec from our target using SOAR speckle imaging data confirming the binary/contaminated nature of this target. We present these three parameters for each of the targets in our sample in Table 2. A full discussion on these parameters and their implications on the candidate dispositions is presented in Section 4.

3 METHODS

3.1 `TFAW` and `TLS`

`TFAW` (del Ser et al. 2018) is a wavelet-based algorithm that is able to denoise and reconstruct the input signal without any *a priori* feature assumption or modify its astrophysical properties. It combines the stationary wavelet transform (hereafter SWT) potential to characterize and denoise the input signal with the detrending and systematic removal capabilities of TFA (Kovács, Zucker & Mazeh 2005).

The `TFAW` detrending and denoising algorithm can be summarized as follows (see del Ser et al. 2018 for a complete description): (1) as with `TFA`, a template of reference stars is used to create an initial filter to remove trends and systematics from the target light curve, (2) using the detrended light curve, the noise-free underlying signal is estimated by means of the SWT decomposition levels and its corresponding power spectrum, (3) outliers are removed based on the previous SWT signal estimation and the high-frequency noise contribution is removed from the target light curve using the SWT decomposition level/s with the highest frequency resolution/s, (4) a search for significant periodicities is run over the denoised signal, (5) if a significant period is found, the detrended and denoised light curve is phase folded and the underlying signal (i.e. the astrophysical signal) is estimated using the SWT, and (6) the final noise-free signal is iteratively denoised and reconstructed.

As shown in del Ser & Fors (2020), `TFAW` delivers both better photometric precision and planet characterization than any previous detrending method applied to *K2* light curves. In order to increase the transit detection potential of the algorithm, we make use of `TLS` during the `TFAW` period search step. `TLS` makes use of the stellar limb-darkening parameters of the target star and includes the effects of planetary ingress and egress in the search for transit-like features. This leads to an increase in the detection efficiency compared to the commonly used `BLS` (Kovács, Zucker & Mazeh 2002) and is particularly suited for the detection of small planets. The combination of `TLS` and `TFAW` can yield detection efficiencies for *K2* data $\sim$8.5 $\times$ higher for `TFAW`-corrected light curves than for `EVEREST 2.0` ones, specially for faint magnitudes (del Ser & Fors 2020).

3.2 Vetting procedure

We follow a transit search, vetting, and false-positive probability (FPP) approach similar to the one detailed in Heller et al. (2019). A candidate period is considered to be significant if its peak in the `TLS` power spectrum during `TFAW` period search step (see Section 3.1) has a signal detection efficiency (SDE_{TLS}) above 9.0 (i.e. false-positive rate $<10^{-4}$ (Hippke & Heller 2019)). Any target light curve that matches these criteria undergoes the full `TFAW` iterative denoising and signal reconstruction. Following the recommendation in Luger et al. (2018), and to avoid any over-fitting of the transit signal by the PLD correction, we mask the candidate transits and recompute their `EVEREST 2.0` light curves prior to rerunning the full `TFAW` correction.

Our vetting procedure consists of the following steps: (1) we visually inspect all `TFAW`-corrected light curves and keep those that have transit-like features. (2) We compare the `TLS` periodograms for the original `EVEREST 2.0` and the `TFAW` light curves to verify that we have not introduced any systematic signature in the data during the `TFAW` analysis. We also compare our results with the available *K2* pipeline and `K2SFF` (Vanderburg & Johnson 2014) light curves, and with PLD-corrected light curves obtained from *K2* TPFs using the `lightkurve` (Lightkurve Collaboration 2018) package. The latter is done with extra care if a nearby star is contaminating the `EVEREST 2.0` aperture. In this case, we check how the transit feature is affected for different aperture sizes and positions. (3) We iteratively run `TLS` to search for extra transiting signals in the light curve. (4) We also rule out that no other light curve in the same CCD module presents transit-like features with similar periods and transit epochs as the candidates. We also check for any systematic bias by plotting the overall distribution of periods in the CCD module and comparing them to our candidate period. (5) Using `TLS` output, we check that all transiting signals have good signal-to-noise ratios (SNR) (long-period candidates should have SNR > 10) and the average depth of the odd/even transits agree within $<3\sigma$, and secondary eclipses at half an orbital phase after the candidate transit are not present at the $>3\sigma$ level. We visually inspect the transits positions in the light curves and require that they are at least 0.5 d away from the beginning or end of any gaps in their light curves to avoid false positives, especially in the case of long period candidates. (6) We cross-match our candidates with the most up-to-date (March 2022) lists of confirmed or candidate exoplanets from the NASA Exoplanet Archive[4] or in the Vizier data base (Adams, Jackson & Endl 2016; Barros, Demangeon & Deleuil 2016; Crossfield et al. 2016; Vanderburg et al. 2016; Crossfield et al. 2018; Hirano et al. 2018; Livingston et al. 2018; Mayo et al. 2018; Dattilo et al. 2019; Kruse et al. 2019; Castro González et al. 2020; Kovacs 2020; Zink et al. 2020; Adams et al. 2021; Castro-González et al. 2021; de Leon et al. 2021; Zink et al. 2021; Christiansen et al. 2022). (7) We run `EDI-Vetter Unplugged`,[5] a simplified version of `EDI-Vetter` (Zink et al. 2020) that uses the output from `TLS` to identify false-positive transit-like signals using a battery of tests: transit outliers, individual transit, even/odd transit, secondary transit, phase coverage, period, and transit duration limits, period alias, and flux contamination checks. (8) Finally, we use high-resolution imaging and *Gaia* photometry and astrometry (see Sections 2.4 and 2.5) to evaluate contamination from other stellar sources.

3.3 Centroid testing

The centroid test (i.e. measuring the changes in the position of the centroid of a target star during the transit) is an excellent tool to discern between bona fide planetary candidates and background transiting sources (Batalha et al. 2010; Bryson et al. 2013) for *Kepler* light curves. After the failure of the second reaction wheel of *Kepler* primary mission in 2013, the *K2* mission relied on the two remaining reaction wheels to balance against the radiation pressure of the Sun. In this way, *K2* was able to reduce the pointing drifts and achieve a photometric precision close to the one for the original *Kepler* mission (Vanderburg & Johnson 2014). However, as the spacecraft continuously and slightly rotated out of position and then was re-adjusted to its original pointing, this resulted in increased correlated noise in the *K2* light curves on time-scales typical of planetary transit durations. Although, some algorithms such as EVEREST 2.0 (which makes use of the PLD technique) were able to correct this effect, some previously validated planets have been found to be background eclipsing binaries (BEBs) near or within the photometric aperture. As a final vetting tool in our procedure, we use vetting (Hedges 2021), a PYTHON-based implementation of the centroid test that takes into account the *K2* motion. It makes use of the *K2* TPF information, the transit period, T_0, and duration to return two distributions of centroids (in transit and out of transit), and a p-value corresponding to the likelihood that they are both drawn from the same underlying distribution. We also pass our transit depths to the code to get the distance to which a companion can be ruled out. We added a modification to the code in order to account for the aperture size used by EVEREST 2.0 as it is usually larger than the one used by the standard *Kepler* pipeline. We use the same threshold for the p-value as Christiansen et al. (2022) to separate between false positives and possible planetary candidates. Only those candidates with $p > 0.05$ are considered vetted planetary candidates.

3.4 Stellar blending

The aperture radius of the EVEREST 2.0 pipeline is usually ∼4 pixels in radius. Given *K2*'s relatively large pixel size (3.98 arcsec), it leads to the possibility of other objects being present within the photometric aperture. This flux contamination leads to a decrease in the observed transit depth, and, as a consequence to biased planetary characterization (Daemgen et al. 2009). As explained in Section 3.2, in those cases where the contaminating object is far enough away from the target star, we recompute the light curve modifying the aperture position and size, and studying whether there is any change in the transit depth. However, in some cases, the object is within a couple of pixels from the target, making it impossible to deblend their flux contributions. For these cases, we quantify the photometric contamination by computing the dilution factor (Daemgen et al. 2009; Livingston et al. 2018) as $\gamma = 1 + 10^{0.4\Delta m}$, where Δm denotes the difference between the magnitude of the fainter contaminating star and the brighter target star in a given photometric band (i.e. the formula assumes the brighter component to be the variable component). The relationship between the observed transit depth (δ arcmin) and the true transit depth (δ) is then given by δ arcmin = $\gamma^{-1}\delta$. Following the notation in Castro-González et al. (2021) and de Leon et al. (2021), we compute the dilution factors γ_{pri} and γ_{sec}, considering that the transiting signal comes from the target (primary) star or from the nearby (secondary) star with transit depths δ_{pri} and δ_{sec}, respectively. Faint eclipsing binaries, when blended, can have their eclipses diluted to depths similar to planetary transit ones. Assuming that their hypothetical eclipses can not be greater than 100 per cent (i.e. $\delta_{\mathrm{sec}} \leq 1$), then if δ arcmin $> \gamma_{\mathrm{sec}}^{-1}$, the observed depth δ arcmin is too deep to be caused by the fainter neighbouring star. We compare these results to the nearby star tests done by TRICERATOPS to decide the final dispositions of those targets with contaminating/blended sources.

3.5 Transit parameters modelling

To model the transit light curves, we use the probabilistic Keplerian Orbit model provided by the exoplanet package (Foreman-Mackey et al. 2021), and a quadratic limb darkening law as parametrized by Kipping (2013) (implemented in exoplanet). As explained in Section 2.2, the limb darkening coefficients are obtained from the tabulated values in Claret (2018). We include a Gaussian Process (GP) model (implemented using celerite2 (Foreman-Mackey et al. 2017; Foreman-Mackey 2018) consisting on a Matérn 3/2 kernel plus a jitter or 'white' noise term to generalize the likelihood function in order to consider correlated noise, non-periodic variations, and to minimize the bias of the inferred parameters. In the case of ultra-short-period (USP) candidates, following Adams et al. (2016), we use super-sampling (7 points for $4 \leq$ period ∼24 hr) to fit the transits given the few observations per transit for very short transit durations.

We assume circular orbits (i.e. eccentricity = 0) and fit the following five transit parameters: the transit epoch, T_0, the orbital period, P, the semimajor axis of the orbit, a, the planetary radius, R_{p}, and the inclination of the orbit, i. We also include as free parameters the stellar radius, the logarithm of the Gaussian errors, a constant light-curve baseline, and the quadratic limb darkening coefficients.

We use the MCMC sampler provided by PyMC3 (Salvatier, Wiecki & Fonnesbeck 2016) to explore the posterior probability distribution. We optimize the model parameters to find the maximum a posteriori (MAP) parameters as a starting point for the MCMC sampler. We consider normal distributions of the priors for all free parameters with the exception of the stellar radius which is bounded by its catalogued uncertainties. We give wide enough bounds to let the chains explore the parameter space without getting close to the bound limit. We run the sampler with 100 walkers, 10 000 iterations with a burn-in phase of 2000 iterations to ensure that each walker runs for more than 50 auto-correlation times for each parameter and the mean acceptance fraction is between 0.25 and 0.5 (Bernardo et al. 1996; Foreman-Mackey et al. 2013). We also inspect the MCMC chains and posterior distributions as well as the final fitted model to ensure they are well-behaved. In Table 3, we report the 50 per cent quantiles as the best-fitting parameters and their upper and lower errors computed from the 25 and 75 per cent quantiles, respectively. The transit light curves and their best-fitting transit model are show in Figs 1 and 2.

3.6 False positive probabilities and validation

Statistical validation, i.e. the statistical confirmation that a transiting signal arises from a planet and not from an astrophysical false positive is a challenging issue. Several planetary transit validation methods have been developed in the literature over the years (Morton 2012; Díaz et al. 2014; Lissauer et al. 2014; Morton 2015a; Torres et al. 2015; Giacalone & Dressing 2020; Armstrong, Gamper & Damoulas 2021; Giacalone et al. 2021) based in different techniques like Bayesian methods or machine learning. vespa (Morton 2012, 2015a) has been largely used to validate planets from the *Kepler* and *K2* missions (e.g. Livingston et al. 2018; Dattilo et al. 2019; Heller et al. 2019; Castro González et al. 2020; de Leon et al. 2021).

Table 3. Candidate MCMC posterior transit parameters, FPPs and dispositions.

EPIC	Name	T_0 (BJD-2454833)	P (d)	a (au)	R_p ($R_\oplus$)	i (°)	$S/S_\oplus$	SDE_{TLS}	FPP_{VESPA}	$FPP_{TRICERATOPS}$	notes	Disposition
205979483.01		$2145.1578^{+0.0016}_{-0.0015}$	$12.4292^{+0.0005}_{-0.0007}$	$0.0974^{+0.0027}_{-0.0031}$	$1.1126^{+0.0450}_{-0.0456}$	$90.000^{+0.3968}_{-0.3960}$	53.836	17.909	–	–		FP/CC
206461841.01		$2149.6596^{+0.0022}_{-0.0024}$	$10.4404^{+0.0007}_{-0.0011}$	$0.0828^{+0.0034}_{-0.0035}$	$0.6739^{+0.0394}_{-0.0370}$	$89.9971^{+0.5356}_{-0.5338}$	41.745	14.324	0.3081	0.1168		PC
210418253.01		$2233.8056^{+0.0017}_{-0.0027}$	$23.9683^{+0.0044}_{-0.0013}$	0.1791 ± 0.0046	$1.6119^{+0.1413}_{-0.1343}$	$91.0247^{+0.1476}_{-1.8806}$	28.046	14.439	0.3004	0.2533		PC
210706310.01		2229.7095 ± 0.0015	5.1718 ± 0.0002	$0.0510^{+0.0024}_{-0.0029}$	$0.8891^{+0.0529}_{-0.0443}$	$90.0307^{+1.5873}_{-1.5942}$	391.097	15.612	0.00239	0.1527		PC
210708830.01		2231.1694 ± 0.0015	5.7408 ± 0.0002	$0.0627^{+0.0026}_{-0.0029}$	$1.0668^{+0.0573}_{-0.0444}$	$89.9948^{+0.9284}_{-0.9156}$	107.349	12.503	0.8392	0.2033		PC
210768568.01	K2-411 b	$2231.8355^{+0.0019}_{-0.0018}$	3.2141 ± 0.0002	$0.0511^{+0.0021}_{-0.0028}$	$0.9898^{+0.0498}_{-0.0486}$	$90.0008^{+2.2467}_{-2.5589}$	619.038	13.63	0.0016	0.015		VP
210945680.01		$2242.5226^{+0.0019}_{-0.0013}$	$20.5949^{+0.0022}_{-0.0010}$	$0.1477^{+0.0047}_{-0.0046}$	$1.5097^{+0.0741}_{-0.0790}$	$89.0790^{+0.2482}_{-0.1533}$	58.550	17.533	0.05459	0.116	★	PC
210967369.01		$2229.4873^{+0.0028}_{-0.0030}$	7.1149 ± 0.0006	$0.0589^{+0.0021}_{-0.0024}$	$0.9835^{+0.0483}_{-0.0499}$	$90.0013^{+0.8089}_{-0.8110}$	220.293	13.245	0.8165	0.266		PC
218701083.01		2471.8892 ± 0.0030	5.0521 ± 0.0004	$0.0529^{+0.0019}_{-0.0022}$	$2.1388^{+0.0898}_{-0.0924}$	$89.9891^{+1.5234}_{-1.5050}$	1073.998	11.81	0	0.3271		FP
220356827.01		$2563.1692^{+0.0038}_{-0.0043}$	4.7535 ± 0.0005	$0.0559^{+0.0034}_{-0.0039}$	$1.5147^{+0.1477}_{-0.1000}$	$89.9707^{+2.4107}_{-2.4000}$	594.594	12.743	0.9834	0.4558		FP/CC
220471100.01		2560.0112 ± 0.0016	$7.3274^{+0.0002}_{-0.0003}$	$0.0760^{+0.0023}_{-0.0026}$	$2.1225^{+0.0731}_{-0.0667}$	$89.9968^{+0.6323}_{-0.6336}$	104.428	26.11	–	–		FP/CC
246022853.01		$2911.3949^{+0.0036}_{-0.0042}$	10.7228 ± 0.0011	$0.0879^{+0.035}_{-0.0037}$	$1.2998^{+0.0689}_{-0.0690}$	$89.9955^{+0.7779}_{-0.7816}$	175.686	10.433	–	–		FP/CC
246048459.01		$2905.6563^{+0.003}_{-0.0023}$	2.0507 ± 0.0001	$0.0258^{+0.0023}_{-0.0025}$	$0.4064^{+0.0302}_{-0.0266}$	$90.0112^{+2.4869}_{-2.5015}$	232.818	10.592	0.3407	0.9836		FP
246078343.01	K2-413 b	$2905.6924^{+0.0017}_{-0.0021}$	0.8094 ± 0.00003	$0.0117^{+0.0009}_{-0.0012}$	$0.7599^{+0.0758}_{-0.0496}$	$89.9518^{+0.6250}_{-6.1473}$	921.755	17.088	6×10^{-4}	0.009		VP
246078343.02	K2-413 c	$2906.1673^{+0.0023}_{-0.0024}$	5.3301 ± 0.0003	$0.0426^{+0.0016}_{-0.0019}$	$1.2327^{+0.0565}_{-0.0593}$	$89.9985^{+0.8243}_{-0.8117}$	69.529	14.329	2×10^{-4}	0.007	†	VP
246163416.01		2905.8554 ± 0.0007	0.8768 ± 0.00002	0.0034 ± 0.0001	$8.4683^{+4.3149}_{-2.8121}$	$140.52^{+2.2073}_{-2.1373}$	4001.692	32.173	–	–		FP/CC
246220667.01	K2-414 b	$2907.2563^{+0.0010}_{-0.0012}$	6.6690 ± 0.0002	$0.0552^{+0.0017}_{-0.0023}$	$1.9287^{+0.0630}_{-0.0728}$	$89.9973^{+0.6830}_{-0.6794}$	56.130	23.962	0.0097	0.0067		VP
246220667.02	K2-414 c	2909.0993 ± 0.0013	4.3696 ± 0.0001	$0.0487^{+0.0027}_{-0.0031}$	$1.2190^{+0.1004}_{-0.0731}$	$90.0045^{+1.3925}_{-1.3991}$	72.113	21.1445	0.001	0.005		VP
247223703.01		$2989.9313^{+0.0092}_{-0.0057}$	3.1764 ± 0.0005	$0.0377^{+0.0048}_{-0.0044}$	$0.9532^{+0.2050}_{-0.2043}$	$89.9893^{+2.1050}_{-2.1043}$	133.976	14.586	0.5567	0.0943		PC
247422570.01	K2-412 b	$2990.1456^{+0.0043}_{-0.0028}$	$5.9382^{+0.0006}_{-0.0004}$	$0.0586^{+0.0032}_{-0.0033}$	$2.1160^{+0.1050}_{-0.1052}$	$89.9980^{+1.3080}_{-1.3214}$	243.518	19.11	0	0.0036		VP
247560727.01		$2989.6718^{+0.0026}_{-0.0019}$	3.3733 ± 0.0002	$0.0279^{+0.0013}_{-0.0016}$	1.5839 ± 0.0781	$89.9954^{+1.7526}_{-1.7522}$	109.437	21.932	0.0013	0.0135		PC/CC
247560727.02		$2993.7254^{+0.0017}_{-0.0018}$	$8.4356^{+0.001}_{-0.0006}$	$0.0708^{+0.0051}_{-0.0056}$	$2.9192^{+0.4080}_{-0.3350}$	$87.5945^{+0.3104}_{-0.3697}$	704.732	14.6306	0.03	0.028		PC/CC
247744801.01		$2994.9350^{+0.0016}_{-0.0018}$	$12.5050^{+0.0007}_{-0.0006}$	$0.1034^{+0.0033}_{-0.0037}$	$1.6730^{+0.0825}_{-0.0772}$	$89.9995^{+0.5221}_{-0.5273}$	58.958	20.705	0.2907	0.2576		PC
247874191.01		$2989.5529^{+0.0007}_{-0.001}$	$7.6240^{+0.0007}_{-0.001}$	$0.0775^{+0.0036}_{-0.0040}$	$2.4551^{+0.1655}_{-0.1378}$	$90.0133^{+1.6828}_{-1.7013}$	321.730	15.903	0.0069	0.0485		PC
211436876.01		$3419.1996^{+0.0101}_{-0.0072}$	$1.1524^{+0.0003}_{-0.0004}$	$0.0125^{+0.0009}_{-0.0011}$	$0.6746^{+0.0454}_{-0.0392}$	$89.9962^{+7.9422}_{-7.9753}$	8270.029	10.786	0.4624	0.1054		PC
211572480.01		3421.2436	6.2043	0.0661	1.8527	–	–	15.46	–	–		FP
211705502.01		3418.7764	2.5819	0.0368	1.9422	–	–	19.917	–	–	*	FP

Note. ★: listed in Zink et al. (2021); †: listed in Dattilo et al. (2019); *: listed in Castro-González et al. (2021).
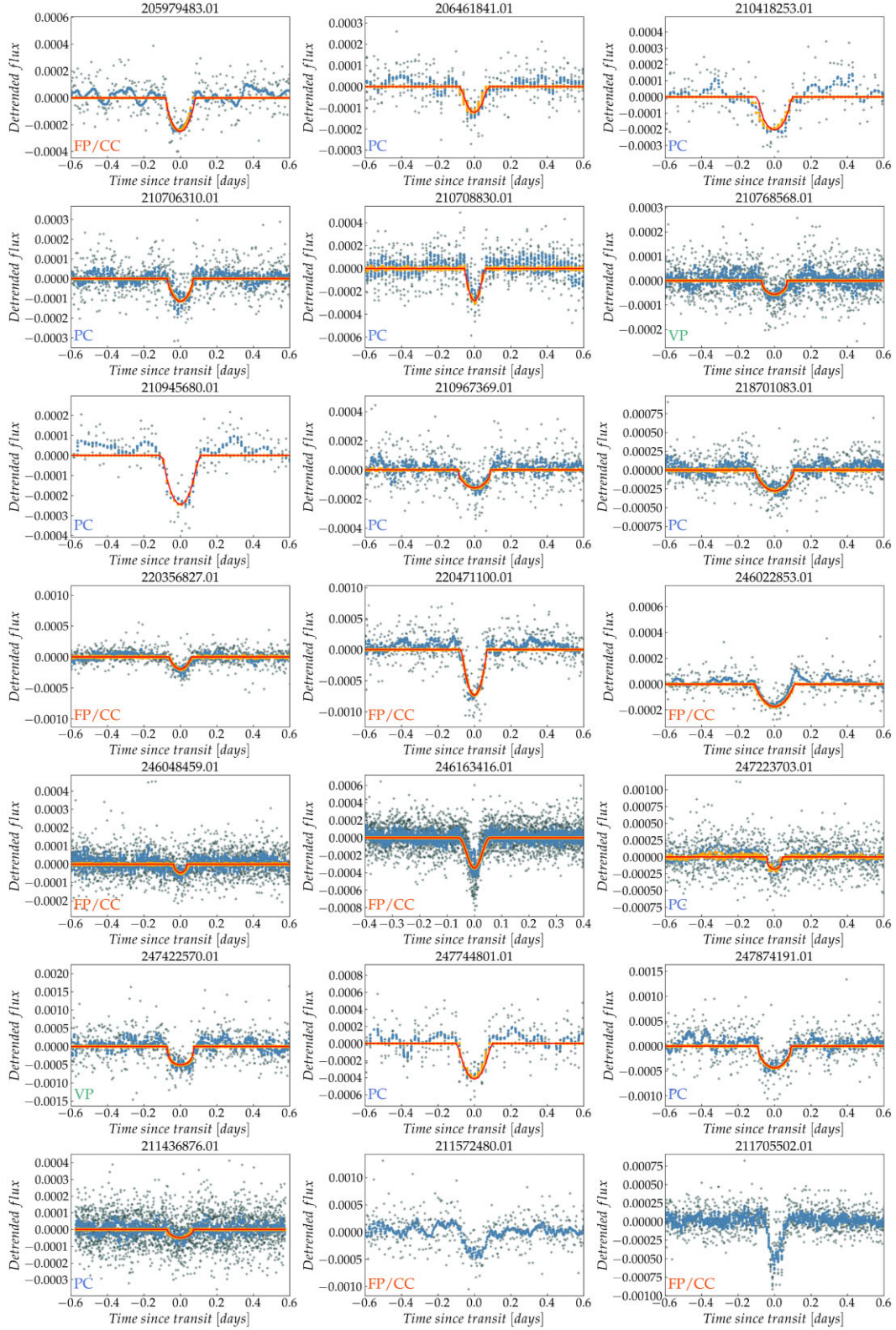
Figure 1. EVEREST 2.0 (grey points), TFAW-corrected (blue points), and TFAW + GP corrected (orange points) light curves and superposed MCMC best-fitting transit model (red line) for all single planet candidates in this work. Final dispositions in the lower left corner (VP = validated planet; PC = planet candidate; FP/CC = false positive/contaminated candidate).
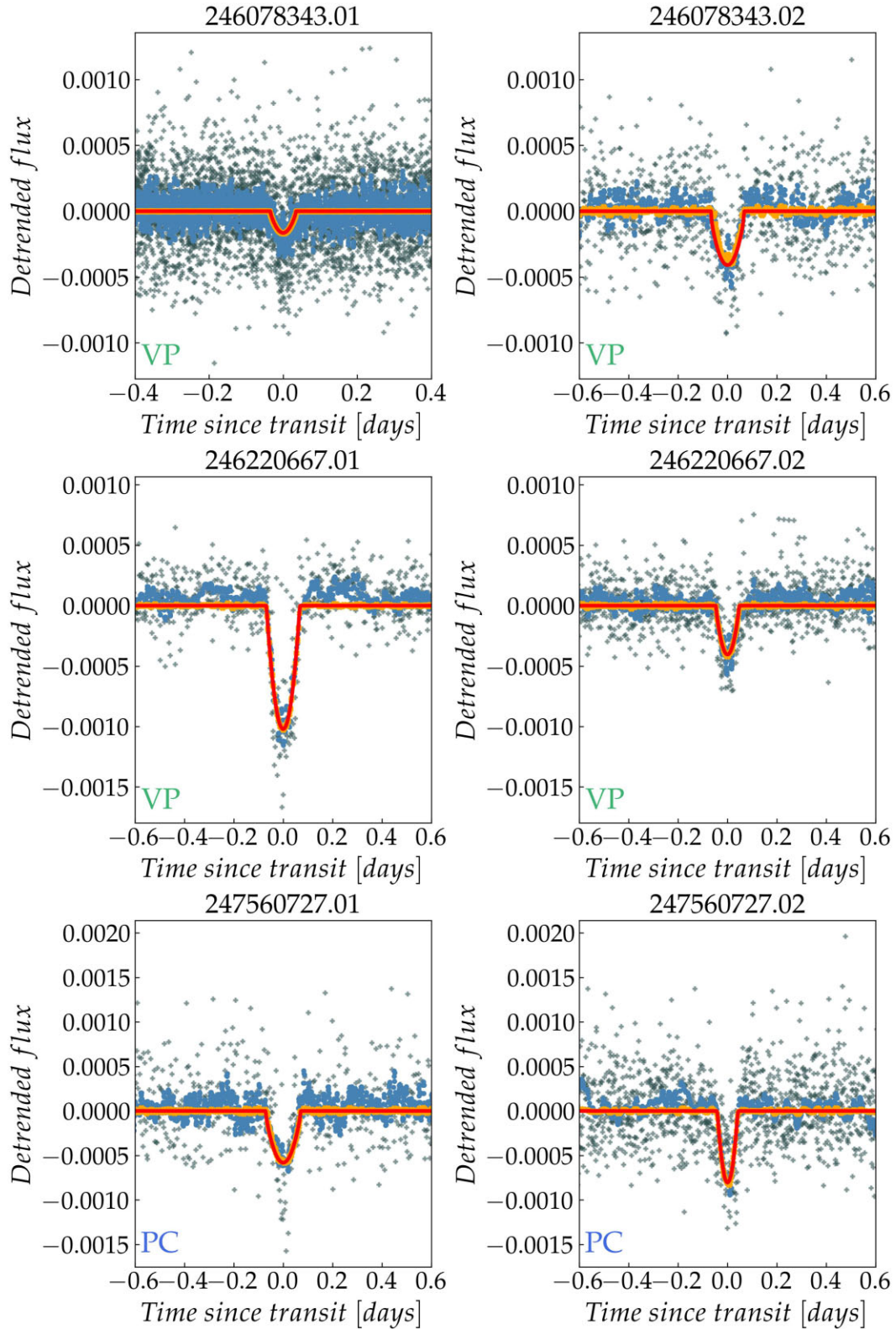
Figure 2. EVEREST 2.0 (grey points), TFAW-corrected (blue points), and TFAW + GP corrected (orange points) light curves and superposed MCMC best-fitting transit model (red line) for all multiplanetary candidates in this work. Final dispositions in the lower left corner (VP = validated planet; PC = planet candidate).

Using the stellar and photometric properties of the host star, `vespa` generates a synthetic sample of stars around the target by means of the `isochrones`[6] package (Morton 2015b). Then, `vespa` calculates the probabilities of the transiting signal being caused by different scenarios: non-associated blended eclipsing binaries, eclipsing binaries, hierarchical triples, non-associated stars with transiting planets, and lastly, the transiting planet scenario around the target star. Planetary candidates with false positive probabilities (FPPs) lower than 1 per cent are considered to be validated planets.

However, Armstrong et al. (2021) find concerning discrepancies with `vespa` and caution against using only one method to validate planetary candidates. The use of independent methods is desirable to reduce the risk of model-dependent biases that could impact several exoplanet research fields and follow-up observations. To minimize the risk of misclassifying our planet candidates, we quantify their FPPs by combining the results from `vespa` with those from `TRICERATOPS` (Giacalone & Dressing 2020; Giacalone et al. 2021). `TRICERATOPS` is a Bayesian tool that vets and validates planet candidates by calculating the probabilities for a set of transit-like scenarios using the target light curve, the photometric aperture, the stellar properties of the host star, and current models of planet occurrence and stellar multiplicities. It also computes the probability that the observed transit comes from a resolved nearby star (denoted nearby FPP or NFPP). A planetary candidate is considered to be validated if they have FPP < 0.015 and NFPP < 10^{-3}.

We supply both software with the `TFAW` phase folded light curves of our candidates, their celestial coordinates, and the stellar parameters and photometric data of their host star. We also compute a limiting aperture radius obtained from the `EVEREST 2.0` information for each star and include the speckle imaging contrast curves (see Section 2.3) as additional constraints. In the particular case of `vespa`, following Mayo et al. (2018), we also include the `secthresh` value, computed using the 3-σ deviation of the out-of-transit phase-folded light curve. This way, we consider the fact that no secondary transit is detected at any phase.

In the case of multiplanetary candidate systems, and given that neither `vespa` nor `TRICERATOPS` consider multiplicity, we apply a correction factor for the computed FPPs to account for the low probability of multiple false-positive signals (Lissauer et al. 2011). Lissauer et al. (2012) introduce correction factors derived from *Kepler* data of ∼25 and ∼50 for systems with two and three or more planets, respectively. Given the different Galactic environments and observational constraints of the *K2* mission, Castro González et al. (2020) computed very similar correction factors of ∼28 and ∼40, based on candidates from several *K2* campaigns.

3.7 Mass-radius estimation and multiplanet resonance analysis

In those stellar systems, in which more than one transiting planet candidate is found, low-order mean motion resonances are estimated using a `PYTHON`-based analytical tool `analytical-resonance-widths`.[7] The algorithm originally uses the Lissauer et al. (2011) mass-radius relationship, based on fitting a power-law relation to the Earth and the Saturn only to estimate the masses of a given multiplanetary system. In our case, we use the `PYTHON`-based `mrexo`[8] tool for non-parametric fitting and analysis of the mass-radius relationship for exoplanets. The code allows to choose

between the mass-radius relationship obtained from the M-dwarf sample data set of Kanodia et al. (2019), and the one obtained using the complete *Kepler* exoplanet sample of Ning, Wolfgang & Ghosh (2018). However, two effects have to be taken into account in order to estimate the masses of planets with $R_p \lesssim 1.2\,R_\oplus$, and to avoid biased results: first, the small amount of Earth-sized planets with a measured mass around FGK dwarf stars, and second, the M-dwarf dataset is strongly affected by the presence of the TRAPPIST-1 planets (Gillon et al. 2017). Thus, for planets with $R_p \lesssim 1.2\,R_\oplus$, we estimate their masses with the widely used programme `FORECASTER`[9] (Chen & Kipping 2016). It uses a broken power law to fit the mass-radius relationship across a wide range of planetary masses and radii to take into account the potential differences in the physical mechanisms responsible for the planetary formation. To estimate the mass of each of our candidate planets, we select the corresponding sample, and algorithm depending on the catalogued spectral types of their host stars (see Section 2.2) and their MCMC best-fitting planetary radius (see Section 3.5).

3.8 Candidate dispositions

Following the vetting and validation procedure described in the previous sections, we assign the final dispositions of each of our candidates. First, those objects with D > 5, `GOF_AL` > 20, and `RUWE` > 1.4 (see Section 2.5) are designated as false positives (FP). If any combination of two of these parameters is above the previous limits, we also consider the target as a FP. Regardless of their values, if a contaminating object is found in the speckle imaging data, we also consider the candidate as a FP.

If a nearby star is found within the `EVEREST 2.0` aperture that cannot be established as a potential nearby eclipsing binary (using *Gaia* astrometric parameters), the candidate is designated as a planet candidate (PC). In the case that the contaminating star is far enough to recompute a new `EVEREST 2.0` aperture minimizing the parasitic flux, the light curve is recomputed to obtain the undiluted depth and the true radius of the planet candidate.

We also adopt an upper limit of $R_p < 8\,R_\oplus$, similar to previous works (Mayo et al. 2018; Giacalone & Dressing 2020; de Leon et al. 2021) to denote possible FPs that can be of brown dwarf or low-mass star origin. Following Kipping (2014), we also check that the MCMC-derived stellar densities are consistent with the ones obtained from the catalogued values. The agreement between these two values is indicative of the transit coming from a planet and not from another astrophysical source.

Finally, we use the FPPs computed by `vespa` and `TRICER-ATOPS` to assign the final disposition of the remaining candidates. Those planets with 1 per cent < FPP$_{vespa}$ and FPP$_{TRICERATOPS}$ < 99 per cent are designated as PC while those with FPP$_{vespa}$ and FPP$_{TRICERATOPS}$ < 1 per cent are designated as validated planets (VP). The final dispositions of each of our candidates and their FPPs are listed in Table 3.

4 RESULTS

Following the vetting and validation procedure described in the previous section, we consider as statistically validated planets to those candidates that have passed all the above-mentioned criteria, i.e. having passed all the vetting tests with no evidence of stellar companions from speckle imaging and *Gaia* photometry, and with

---

[6] https://isochrones.readthedocs.io/en/latest/
[7] https://github.com/katvolk/analytical-resonance-widths
[8] https://github.com/shbhuk/mrexo

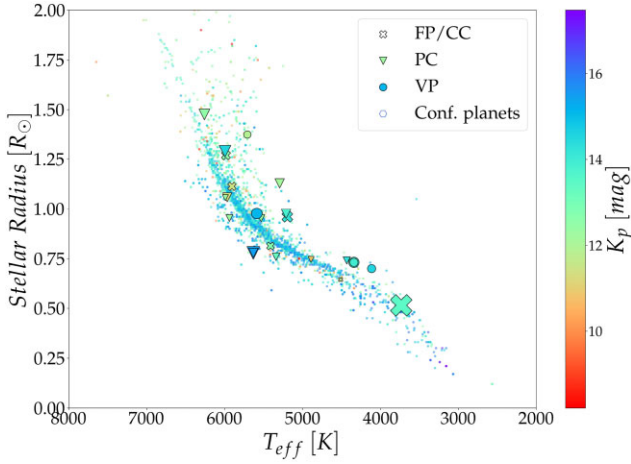[9] https://github.com/chenjj2/forecaster

Figure 3. Distribution of the host stars of our validated (circles), candidate (triangles), and false positive (crosses) sample versus the stellar properties of the hosts stars of know planets from the NASA Exoplanet Archive (hexagons). The sizes of the markers from our sample are scaled to the MCMC best-fitting planetary radius.
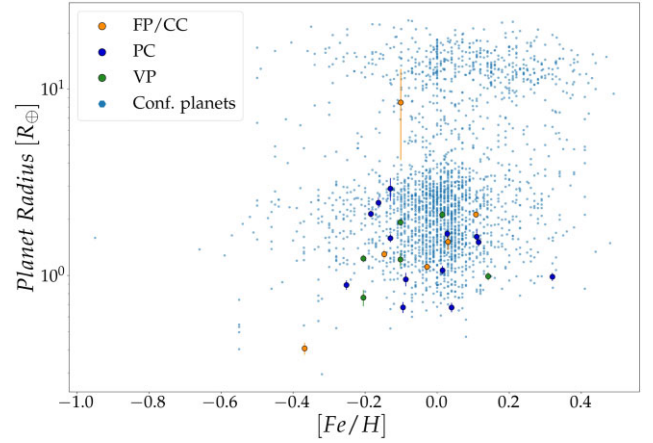

Figure 4. Planetary radius and host star metallicity distribution for our validated (green points), candidate (dark blue points), and false positive (orange points) sample versus the same distribution for confirmed planets with measured radius (blue hexagons) from the NASA Exoplanet Archive.

FPP_{vespa} and $FPP_{TRICERATOPS} < 1$ per cent. From a total sample of 27 candidates in 24 systems (see Table 3), we statistically validate six planets in four different stellar systems: a highly-irradiated the Earth (K2-411 b), a sub-Neptune (K2-412 b) orbiting a G4 star, a two-planet system (K2-413) consisting of a super-Earth (K2-413 c) and a USP planet (K2-413 b) with a similar structure to the Mercury's interior. Also, a super-Earth (K2-414 b) and a sub-Neptune (K2-414 c) pair orbiting close to their 3:2 mean resonance motion around a K5 star. All, except K2-413 c (listed in Dattilo et al. 2019), are new detections missed by previous works. We do a more extended description of these validated systems in Section 4.3. Out of the remaining systems, we present 13 new planet candidates. We highlight EPIC 247560727 (see Section 4.4.1), a multiplanetary candidate system consisting of a super-Earth and sub-Neptune pair in a 5:2 resonant orbit, and EPIC 21436876.01 (see Section 4.4.2) a very-short period sub-Earth around a G2 star. The phase folded light curves with their MCMC best-fitting transit models are shown in Figs 1 and 2. The stellar properties of our host star sample are represented in Fig. 3.

4.1 Characteristics of our host star sample

Our candidate host star sample (see Table 2) has a median magnitude of $K_p = 13.3$, that is ~ 0.7 magnitudes fainter than the median K_p magnitude for the $K2$ confirmed planets host stars ($K_p = 12.5$). They comprise a small fraction of the TFAW survey sample (del Alcázar, del Ser & Fors 2021) (~ 10 per cent) and have been selected in part for being bright enough to have good contrast in speckle imaging detection limit curves. Regarding their spectral types, 10 of our targets are G-type stars, six are K-type stars, three are F-type stars, one is an M-type star, and four of them are missing their spectral classification. Most of our validated and candidate planets are located in less populated areas of the confirmed planet host stellar radius versus T_{eff} diagram (see Fig. 3). In addition, the sub-Earth planetary candidate EPIC 210706310.01 (see Section 4.4.3 for a detailed discussion) seems to orbit a metal-poor host star ([Fe/H] $= -0.402 \pm 0.235$ [dex], Hardegree-Ullman et al. (2020); [Fe/H] $= -0.463428^{+0.35536}_{-0.230723}$ [dex], Anders et al. (2022); [Fe/H] $= -0.252370 \pm 0.081465$ [dex], Buder et al. 2021) (see Fig. 4).

4.2 Characteristics of our planetary sample

4.2.1 Planet period distribution

Fig. 5 shows the orbital period distribution of our validated candidate and false-positive sample. Most of our candidates lie in the $P = \sim 3$–10 d range. Given the length of the $K2$ observing campaigns, these values do not differ from the typical distribution of the confirmed candidate $K2$ sample. Two of our planet candidates (EPIC 210418253.01 and EPIC 210945680.01) have periods larger than 20 d. We remark that in the case of EPIC 210945680.01 (which appears listed as a planet candidate in Zink et al. 2021), although it fails the centroid test (see Fig. 8), we leave it as a planet candidate given that the *Gaia* astrometric parameters are below the thresholds defined in Section 2.5, and we do not detect contaminating sources from BTA speckle observations (but future observations might help in the characterization of this candidate). Although, the occurrence of sub-Neptune planets, as a function of period, changes at ~ 10 d (Winn, Sanchis-Ojeda & Rappaport 2018), USP planets can be defined by the criteria of having a period shorter than ~ 1 d (Adams et al. 2016; Winn et al. 2018). The occurrence rate of USP planets is dependent on the spectral type of the host star, being highest in M-type (1.1 ± 0.4 per cent) and lowest in F-type (0.15 ± 0.05 per cent) (Winn et al. 2018). The origin of the USP population is still not clear with different formation scenarios proposed (see Uzsoy, Rogers & Price 2021, and references within). All the USP planets known so far are either the hot Jupiter or apparently rocky planets (Hamer & Schlaufman 2020; Uzsoy et al. 2021). One of our validated planets (K2-413 b) and one planet candidate (EPIC 211436876.01) have periods ($P = 0.8094 \pm 0.00003$ d and $P = 1.1524^{+0.0003}_{-0.0004}$ d, respectively) that allow us to characterize them as USP planets. For a more detailed discussion on our USP sample, see Sections 4.3.3 and 4.4.2.

4.2.2 Planet radius distribution

Using a planet radius distribution similar to the one from Borucki et al. (2011), our sample of validated and candidate planets (see Fig. 5) is comprised of three sub-Earth planets ($R_p < 0.8 R_{\oplus}$), seven Earths ($0.8 R_{\oplus} \leq R_p < 1.25 R_{\oplus}$), four super-Earths ($1.25 R_{\oplus} \leq R_p < 2 R_{\oplus}$), and four sub-Neptunes ($R_p < 4 R_{\oplus}$).
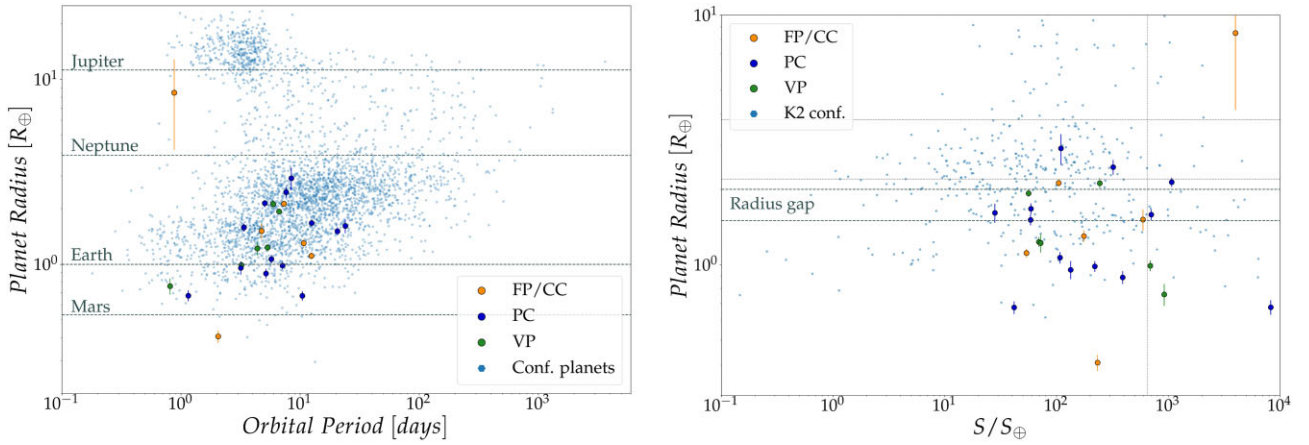
Figure 5. *Left:* Planet radius as a function of the orbital period for our validated planets (green points), planet candidates (dark blue points), and false positive (orange points) sample versus the distribution of confirmed planets (blue hexagons) from NASA Exoplanet Archive. *Right:* Planet radius as a function of the stellar insolation (same notation as left plot). Dark dashed lines denote the approximate location of the Radius Gap. The region enclosed by the light dashed lines at the right of the plot denotes the hot Neptune desert.

Planets with radii $<2 R_\oplus$ are most likely rocky planets; however, the internal nature of planets with $2 R_\oplus < R_p < 4 R_\oplus$ is still a matter of debate. The two most accepted scenarios are that they might either be planets with a rocky core and a gaseous envelope or water worlds (Zeng et al. 2019). This bimodality of the distribution of small planets is separated by an observed scarcity of planets with radii $1.5 R_\oplus < R_p < 2 R_\oplus$ known as the Radius Gap (Fulton et al. 2017). Several scenarios for the Radius Gap origin have been postulated (Owen & Wu 2013, 2017; Venturini & Helled 2017; Ginzburg, Schlichting & Sari 2018; Zeng et al. 2019). In addition, the Radius Gap seems to depend on the stellar host type (Fulton et al. 2017; Zeng, Jacobsen & Sasselov 2017; McDonald, Kreidberg & Lopez 2019) and metallicity, and evolves (as well as the whole planetary radius distribution) on a long time-scale of giga-years (Chen et al. 2022; Petigura et al. 2022). Thus, planets within the Radius Gap can serve as valuable probes to analyse the processes that lead to planet formation, atmosphere loss, and evolution (Petigura 2020). Four of our planet candidates (EPIC 210418253.01, EPIC 210945680.01, EPIC 247744801.01,[10] and EPIC 247560727.01) and one validated planet (K2-414 c) lie within the Radius Gap based on our analysis. Also, eight out of our sample of 18 validated and candidate planets have radii smaller than that of the Radius Gap. This points towards the improved detection of smaller planets by the combination of the TFAW corrected light curves and TLS (del Ser & Fors 2020) in contrast with previous works (Castro-González et al. 2021).

According to the photoevaporation-driven mass-loss model, the planet's atmosphere is heated, stripped off, and driven out by the host star high-energy radiation, leaving the rocky cores (Owen & Wu 2013, 2017). Planets with thicker H/He envelopes may still keep part of it after the first 100 Myr of the host star's lifetime when the high-energy radiation shuts down (Ribas et al. 2005). The remaining atmosphere can significantly inflate the planet's radii and place them in the $R_p > 2 R_\oplus$ part of the observed radii distribution. We analyse whether our four sub-Neptune candidates (i.e. with $2 R_\oplus < R_p < 4 R_\oplus$) can keep an atmospheric envelope over the first billion-year of their host star. Using the equations from Zeng et al. (2019), we

[10]This candidate is affected by the presence of a nearby ($\sim$7.7 arcsec), fainter ($G = 17.51$ mag), star (GOF_AL = 1.79, D = 1.59, RUWE = 1.06).

can estimate the atmospheric components that our candidate planets can hold. These estimates are obtained following the correlation that the escape velocities and the atmospheric composition of Solar system bodies have with the atmospheric escape. We use the masses estimated using the procedure explained in Section 3.7 to derive both the escape velocities ($v_{esc} = \sqrt{2 G M_p R_p^{-1}}$), and planet bulk densities ($\rho = M_p/(4/3\pi R_p^3)$). We compute the surface equilibrium temperatures of our planet sample using the stellar radii, and T_{eff} listed in Table 2, the MCMC best-fitting value for the semimajor axis of the planetary orbit, and we assume a bolometric albedo $A_B = 0.3$, similar to that of the Earth and the Neptune. In Fig. 6, we show the escape velocities of our $R_p < 4 R_\oplus$ validated and candidate planet sample as a function of their surface equilibrium temperatures. We find a clear differentiation between our Earth- and sub-Earth-sized planets and our sub-Neptune sample. The first group seems to be rocky worlds consisting primarily of Mg-silicate-rock and (Fe, Ni)-metal (Zeng et al. 2019), having similar bulk densities to those of the Earth and the Venus. Validated planet, K2-413 b, and planet candidate EPIC 211436876.01 would be rocky planets with a composition similar to that of the Mercury. Our sub-Neptune sample lies within a region with escape velocities of $\sim$20 km s^{-1}, and equilibrium temperatures between 500 and 1500 K. Inside this region, they are susceptible to the escape of H_2 and He and, except for the presence of an internal reservoir, they would not be able to retain their primordial H/He atmospheres during the first Myrs. Zeng et al. (2019) infer that the He escape threshold is the boundary separating the populations of the puffy hot Saturn and smaller planets. More interestingly, our four planet candidates and the one validated planet lying in the Radius Gap, correspond to the five planets closer to the He boundary in Fig. 6. Given their estimated densities, all would be rocky planets, except for EPIC 247560727.02, which would probably be a water world given its estimated bulk density and equilibrium temperature (Zeng et al. 2019).

The photoevaporation desert or the Neptunian desert is a lack of planets between $2-4 R_\oplus$ at very high insolations ($S/S_\oplus > 650$) (Lundkvist et al. 2016; West et al. 2019). The mechanism, be it photoevaporation or core-powered mass loss, giving birth to the observed Neptunian Desert is currently unknown. Thus, planets found in and near the Neptune Desert boundaries are particularly valuable for the understanding of the origin of this phenomenon. Our
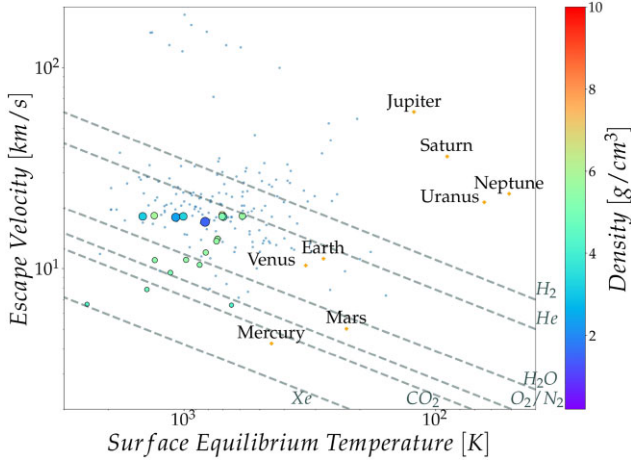
Figure 6. Atmospheric escape velocities versus surface equilibrium temperature for our sample of validated and candidate planets with $R_p < 4 R_\oplus$ (black-edged points) versus. Their face colours correspond to their bulk densities computed from the estimated masses computed as per Section 3.7. For comparison purposes, Solar system bodies (orange crosses), and the confirmed planet (blue hexagons) from the NASA Exoplanet Archive is also plotted. Dashed lines represent the threshold velocities of the atmospheric components labelled at each line.

planet candidate EPIC 218701083.01 with $R_p = 2.1388^{+0.0898}_{-0.0924} R_\oplus$ and $S/S_\oplus = 1073.998$ lies close to the edge of the Neptunian Desert. We find a slightly smaller planetary radius than the one reported in Zink et al. (2021) ($R_p = 2.594^{+0.173}_{-0.186} R_\oplus$). However, we cannot fully validate this candidate due to the presence of several fainter stars within the EVEREST 2.0 photometric aperture (see Fig. 14). Using lightkurve, we have tried to minimize the effects of the neighbouring stars by modifying the photometric aperture and recomputing the light curve. In addition, by checking the *Gaia* astrometric parameters (see Section 2.5) of those stars still within the photometric aperture, we can rule out up to a certain limit, the possibility of them being background eclipsing binaries. A comparison of the *Gaia* astrometric parameters for EPIC 218701083 and the nearest background contaminating stars is listed in Table 4. Given the dilution in the transit depth due to the presence of these contaminating stars (especially from the brightest one, EPIC 218701831), if EPIC 218701083 is the transiting star, the real radius of the planet would be larger than the reported one (taking only EPIC 218701831 as secondary source, then $\gamma_{pri} \sim 1.06$ and $R_p \sim 2.2 R_\oplus$). This could put it inside the Neptunian Desert region (see Fig. 5). However, the background eclipsing binary scenario cannot be fully discarded without further observations.

4.2.3 Habitability analysis

In order to assess whether any of our validated or candidate planets could be in the habitable zone (HZ) of their host stars, we used the polynomial equations from Kopparapu et al. (2013) to determine the limits of the HZ. The conservative HZ is delimited by the 'moist greenhouse' limit ($S/S_\oplus = 1.01$; i.e. where the stratosphere becomes saturated by water and hydrogen begins to escape into space), and the 'maximum greenhouse' limit ($S/S_\oplus = 0.35$; i.e. where the greenhouse effect fails as CO_2 begins to condensate from the atmosphere and the surface becomes too cold to hold liquid water). The optimistic HZ is delimited empirically by the recent Venus and the early Mars' limits, i.e. set by the last time that liquid surface water could have existed on the Venus and the Mars: $S/S_\oplus = 1.78$ and $S/S_\oplus = 0.32$, respectively (Kasting 1988). We also include more optimistic HZ set by Zsom et al. (2013). It takes into account that the HZ for hot desert worlds (1 per cent relative humidity and terrestrial albedo, $A_B = 0.8$, and assuming a surface pressure of 1 bar and a 10^{-4} CO_2 mixing ratio) could be much closer to the star (as close as 0.38 au around a solar-like star). Given the short orbital periods (typical of most of the *K2* confirmed planets) of our candidate sample, and the effective temperatures of our host stars, none of the planets shown in this work are within the HZs discussed above (see Fig. 7).

4.3 Validated planets

4.3.1 EPIC 210768568.01

K2-411 b is an Earth-sized planet ($R = 0.9898^{+0.0498}_{-0.0486} R_\oplus$) orbiting around a relatively bright ($K_p = 11.935$ mag, $G = 11.979$ mag, $J = 10.704$ mag) star ($1.375 \pm 0.068 R_\odot$, $1.018 \pm 0.131 M_\odot$) (Paegert et al. 2021), observed by the *K2* mission during the C4 campaign. Its coordinates are (α, δ) (J2000) = (03:52:00.83, 19:23:28.26), and it is located at a distance of 296 pc (Bailer-Jones et al. 2021). K2-411 b has an orbital semimajor axis of $0.0511^{+0.0021}_{-0.0028}$ au, with a period of 3.2141 ± 0.0002 d, receiving a stellar insolation of $\sim 914 S/S_\oplus$. There is a nearby (~ 20.4 arcsec) fainter ($K_p = 16.689$ mag) star partially affecting the EVEREST 2.0 aperture. Following the vetting procedure explained in Section 3.2, we do not detect changes in the transit depth while modifying the aperture size to diminish the flux from the neighbouring star. The vespa and TRICERATOPS FPP values are 0.0016 and 0.015, respectively. The centroid p-value for this target is 0.569 (see Fig. 8), which is consistent with the target star being the source of the transiting signal. Also, the maximum computed separation that a background eclipsing binary could be at is 6.76 arcsec. We do not detect any companion star at closer separations using speckle imaging data from SOAR and BTA. Using the *Kepler* sample mass-radius relationship from Kanodia et al. (2019), we predict a planetary mass of $\sim 2.34 M_\oplus$, which results in a RV semi-amplitude of $K \sim 1$ m s^{-1}, that is close to the detection

Table 4. Comparison of the *Gaia* eDR3 astrometric properties for EPIC 218701083 and contaminating background stars.

EPIC	*Gaia* eDR3	G [mag]	GOF_AL	D	RUWE
218701083	4098469552910806272	12.54	− 1.43	0.85	0.93
218701831	4098469557255647616	15.92	− 0.52	0	0.97
218700307	4098469522895908480	18.25	0.55	0	1.03
–	4098470313134530944	19.90	0.58	1.11	1.03
–	4098470313133032576	18.39	2.37	0.58	1.13
–	4098469557218787456	18.44	1.58	1.07	1.09
–	4098469557255646720	18.08	0.23	0.29	1.01
–	4098469557255646592	20.47	− 1.06	0	–

Table 5. Comparison of *Gaia* properties for EPIC 247422570 and contaminating nearby stars.

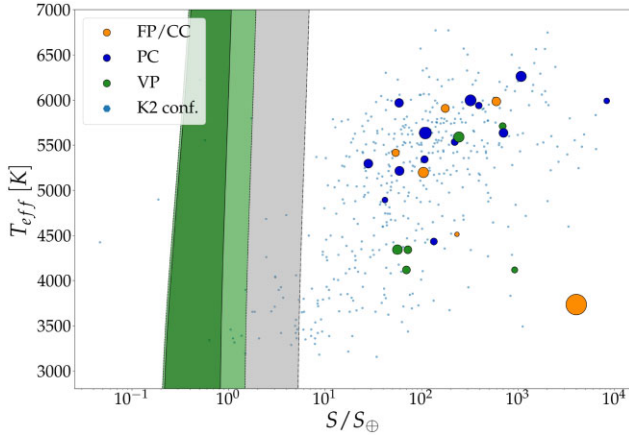| EPIC	*Gaia* eDR3	G [mag]	GOF_AL	D	RUWE
247422570	3409152693750235008	15.13	1.21	0.00	1.05
–	3409152629326319744	20.88	1.33	1.26	–
–	3409152625030757888	19.09	− 0.65	0.00	0.97

Figure 7. Stellar effective temperature as a function of the insolation fluxes received by our validated (green dots), candidate (dark blue dots), and false-positive (orange dots) sample versus the *K2* confirmed sample from NASA Exoplanet Archive (blue hexagons). Dot sizes from our sample candidates are scaled to their MCMC best-fitting planetary radii. The conservative HZ (dark green region) is limited by the two solid lines corresponding to the moist greenhouse inner edge and the maximum greenhouse outer edge. The optimistic HZ (light green region) is bounded by two dashed lines corresponding to the recent Venus inner limit and the early Mars' outer limit. The Zsom et al. (2013) hot desert world HZ (grey region) is limited by the dotted line.

limits of spectrographs like CARMENES (Quirrenbach et al. 2010) and ESPRESSO (Pepe et al. 2010).

4.3.2 EPIC 247422570.01

K2-412 b is a sub-Neptune planet ($R_p = 2.1160^{+0.1050}_{-0.1052} R_\oplus$) orbiting a faint ($K_p = 15.160$ mag, $G = 15.133$ mag, $J = 13.154$ mag) G4 star ($0.977^{+0.066}_{-0.063} R_\odot$, $0.893^{+0.406}_{-0.275} M_\odot$; Hardegree-Ullman et al. 2020) observed during *K2* campaign C13. It is located at (α, δ) (J2000) $= (05:05:02.92, 21:34:48.55)$ at a distance of $\sim$669 pc (Bailer-Jones et al. 2021). K2-412 b orbits its star at a distance of $0.0586^{+0.0032}_{-0.0033}$ au with a period of $5.9382^{+0.0006}_{-0.0004}$ d, receiving a stellar insolation of $\sim$243 $S/S_\oplus$. There are two nearby ($\sim$11 and $\sim$16 arcsec) fainter ($G = 20.885$ and 19.088 mag) stars (see Table 5) partially within the EVEREST 2.0 aperture. Following our vetting procedure, we have modified the photometric aperture to minimize the contamination from these two neighbouring stars. In this case, changing the aperture, we did not detect any significant changes in the transit depth. Also, the light curve obtained using lightkurve and centring a smaller aperture at the position of the fainter neighbouring stars does not produce a transiting feature at the listed period. In addition, the centroid p-value for this target is 0.364 and the maximum computed separation for a background eclipsing binary is 3.7 arcsec (see Fig. 8). Given that this distance is smaller than the angular separation of the neighbouring stars, and the fact that we do not detect any other source with BTA speckle data, we consider K2-

412 to be the host star of this transiting exoplanet. vespa returns a FPP = 0 and TRICERATOPS returns a FPP of $\sim$4 × 10^{-3}. Using the *Kepler* sample from Kanodia et al. (2019), we predict a planetary mass of $\sim$5.58 $M_\oplus$.

4.3.3 EPIC 246078343.01 and EPIC 246078343.02

K2-413 is a faint ($K_p = 14.557$ mag, $G = 14.565$ mag, $J = 12.644$ mag) K7 star ($0.700^{+0.055}_{-0.048} R_\odot$, $0.808^{+0.364}_{-0.256} M_\odot$; Hardegree-Ullman et al. 2020) observed during *K2* campaigns C12 and C19. It is located at (α, δ) (J2000) $= (23:33:40.22, -07:36:42.98)$ at a distance of $\sim$253 pc (Bailer-Jones et al. 2021). It is orbited by two planets: K2-413 b is a sub-Earth USP planet ($0.7599^{+0.0758}_{-0.0496} R_\oplus$) with an orbital semimajor axis of $0.0117^{+0.0009}_{-0.0012}$ au, and a period of 0.8094 ± 0.00003 d. It has a vespa FPP value of 6 × 10^{-4} and a TRICERATOPS FPP of 0.009 after applying the multiplicity boost. Using the mass-radius estimation from Chen & Kipping (2016), we predict a planetary mass of $\sim$0.36 $M_\oplus$. With these planetary parameters, K2-413 b would be a planet with a similar structure to the Mercury's interior, as GJ 367 b (Lam et al. 2021). Also, the presence of a second planet in the system is to be expected given that USP planets are typically accompanied by other planets with orbital periods between 1–50 d (Sanchis-Ojeda et al. 2014). K2-413 c is a $1.2327^{+0.0565}_{-0.0593} R_\oplus$ super-Earth planet orbiting at a distance of $0.0426^{+0.0016}_{-0.0019}$ au with a period of 5.3301 ± 0.0003 d. It was first reported by Dattilo et al. (2019), as a candidate planet in a 5.3288 d orbit in their *K2* planet candidate training/test set. We detect this planet in *K2* C12 EVEREST 2.0 and TFAW light curves, and also, as part of our vetting procedure in the K2SFF one. Given the shorter length ($\sim$6 d) of the good quality data points for the C19 campaign, we are not able to detect the planet using the available light curves. It has a vespa FPP value of 2 × 10^{-4} and a TRICERATOPS FPP value of 0.007, after applying the multiplicity boost, and the available LDT contrast curves, as explained in Section 3.6. The centroid p-values for both planets are 0.468 and 0.676, and the nearest background source would be at distances 8.59 and 5.03 arcsec, respectively (see Fig. 9). In both cases, they are consistent with the target star being the source of the transiting signals. Using the mass-radius estimation from Chen & Kipping (2016), we calculate a planetary mass of $\sim$1.83 $M_\oplus$. Given the orbital periods of these two planets, we do not obtain resonant orbits in this system (see Fig. 10).

4.3.4 EPIC 246220667.01 and EPIC 246220667.02

K2-414 is a faint ($K_p = 13.977$ mag, $G = 13.929$ mag, $J = 12.184$ mag), K5 star ($0.732^{+0.055}_{-0.052} R_\odot$, $0.814^{+0.363}_{-0.251} M_\odot$; Hardegree-Ullman et al. 2020) observed during *K2* campaigns C12 and C19. It is located at (α, δ) (J2000) $= (23:26:32.7, -04:36:23.69)$ at a distance of $\sim$256 pc (Bailer-Jones et al. 2021). It is a multiplanetary system consisting of two planets: K2-414 b with a period of 4.3606 ± 0.0001, and K2-414 c with 6.6690 ± 0.0002 d. With the reported periods, they seem to be close to their 3:2 resonance (see Fig. 11). Although
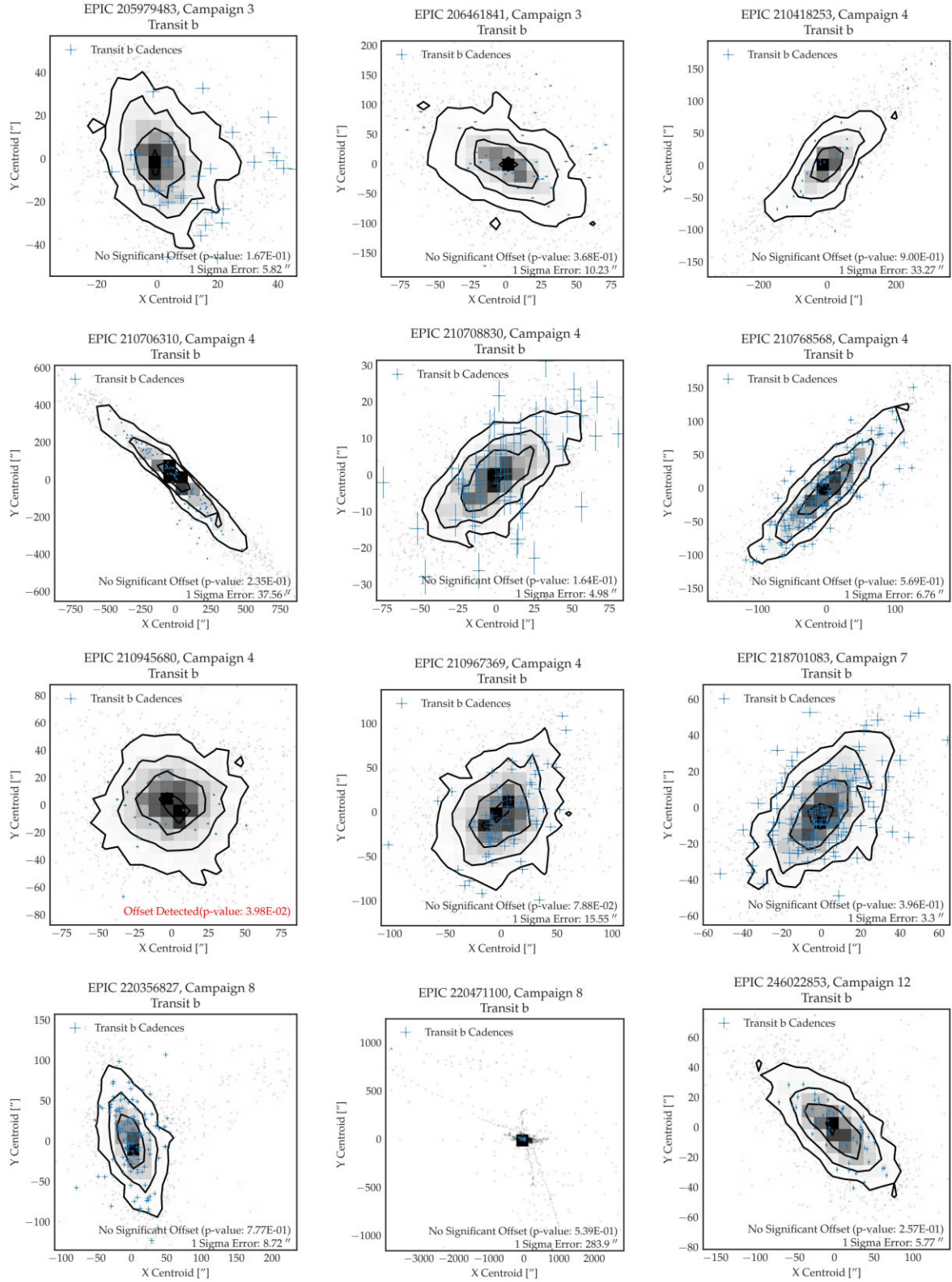
Figure 8. Centroid plots for all single planet candidates listed in Table 3. The in-transit cadences centroid locations are denoted in blue, while the out-of-transit centroid locations are denoted in grey. The 1σ, 2σ, and 3σ contours of the centroids of the out-of-transit cadences are also represented. Candidates with significant centroid offsets (p-value < 0.05) are denoted in red.
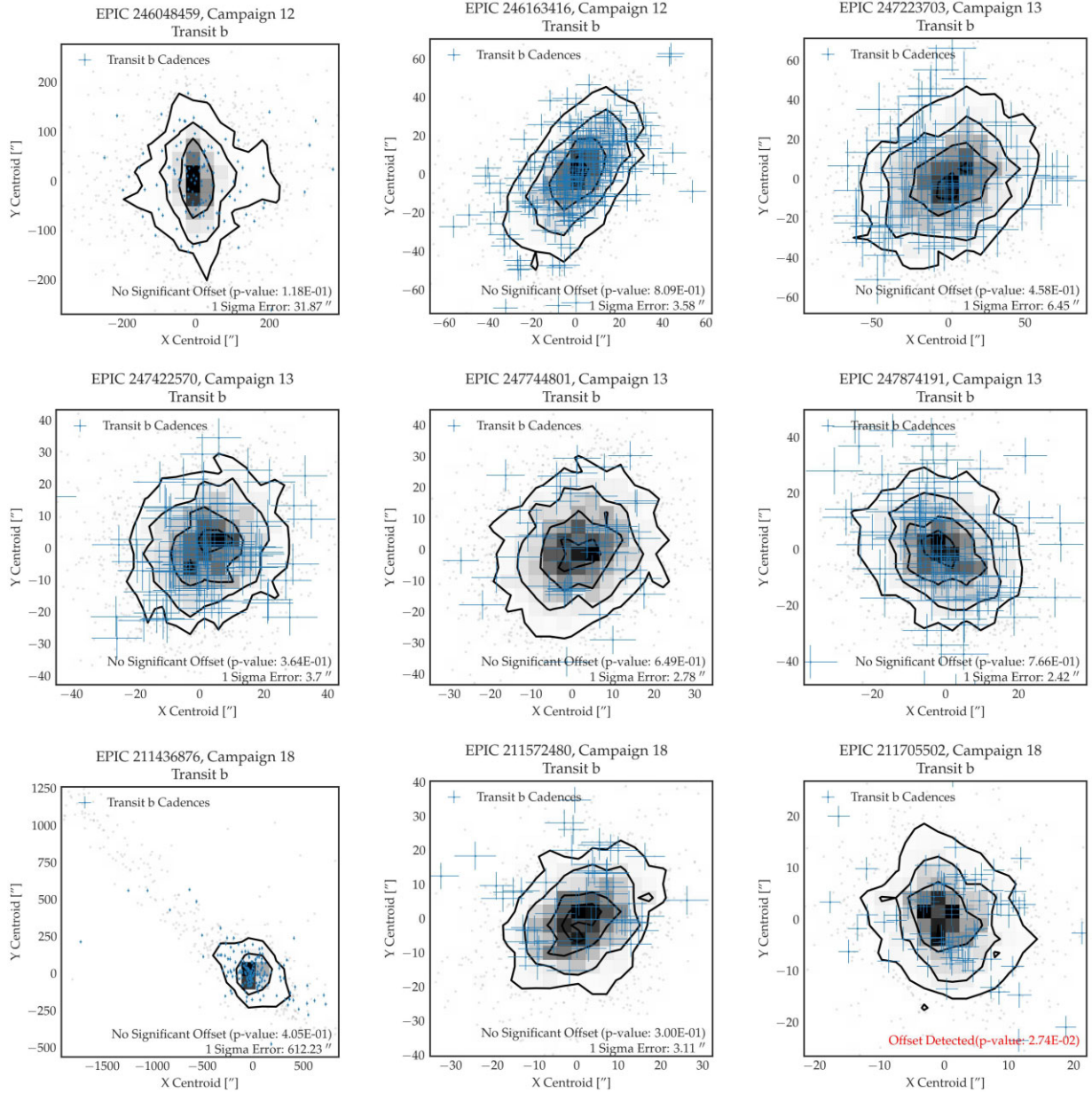
Figure 8 *– continued*

campaign C19 was not considered in our TFAW survey (as there is no EVEREST 2.0 light curve available for this campaign) during our vetting procedure, we searched for these two planets in the available C19 light curves for this system. We detect one transit of K2-414 c in the K2SFF light curve as well as two transits from the TPF light curve obtained using the lightkurve package. We also detect a transit-like feature in the phase-folded K2SFF light curve for K2-414 b. K2-414 b is a validated super-Earth planet ($1.2191^{+0.0993}_{-0.0731} R_{\oplus}$) orbiting its host star at a distance of $0.0487^{+0.0027}_{-0.0031}$ au. It has vespa and TRICERATOPS FPP values of 0.97 and 0.67 per cent, respectively, after the multiplicity boost is applied. Using the mass-radius estimation from Chen & Kipping (2016), we compute a planetary mass of $\sim 1.82 M_{\oplus}$.

K2-414 c is a validated sub-Neptune planet ($1.9288^{+0.0621}_{-0.0719} R_{\oplus}$), orbiting its host star at a distance of $0.0552^{+0.0017}_{-0.0023}$ au. In this case,

given the transit depth (~ 1 ppt) of K2-414 c, the original EVEREST 2.0 light curve presented trimmed transits. We recomputed the EVEREST 2.0 light curve by masking the transit and re-running the PLD analysis to ensure unbiased results of the planetary radius. The vespa and TRICERATOPS FPP values for this planet are 10^{-3} and 5×10^{-3} with the multiplicity boost applied. Using the *Kepler* sample from Kanodia et al. (2019), the estimated planetary mass is $\sim 5.03 M_{\oplus}$. With an incident flux of $\sim 56.13 S/S_{\oplus}$, K2-414 c lies at the upper edge of the Radius Gap for a K-type star (Fulton et al. 2017; Zeng et al. 2017; Petigura et al. 2022).

The centroid p-values are 0.458 and 0.867, and the distances to the nearest background sources are 38.87 and 18.75 arcsec, respectively (see Fig. 9). We do not detect any contaminating source within these distances neither with *Gaia* eDR3 data nor with our LDT speckle imaging observations.
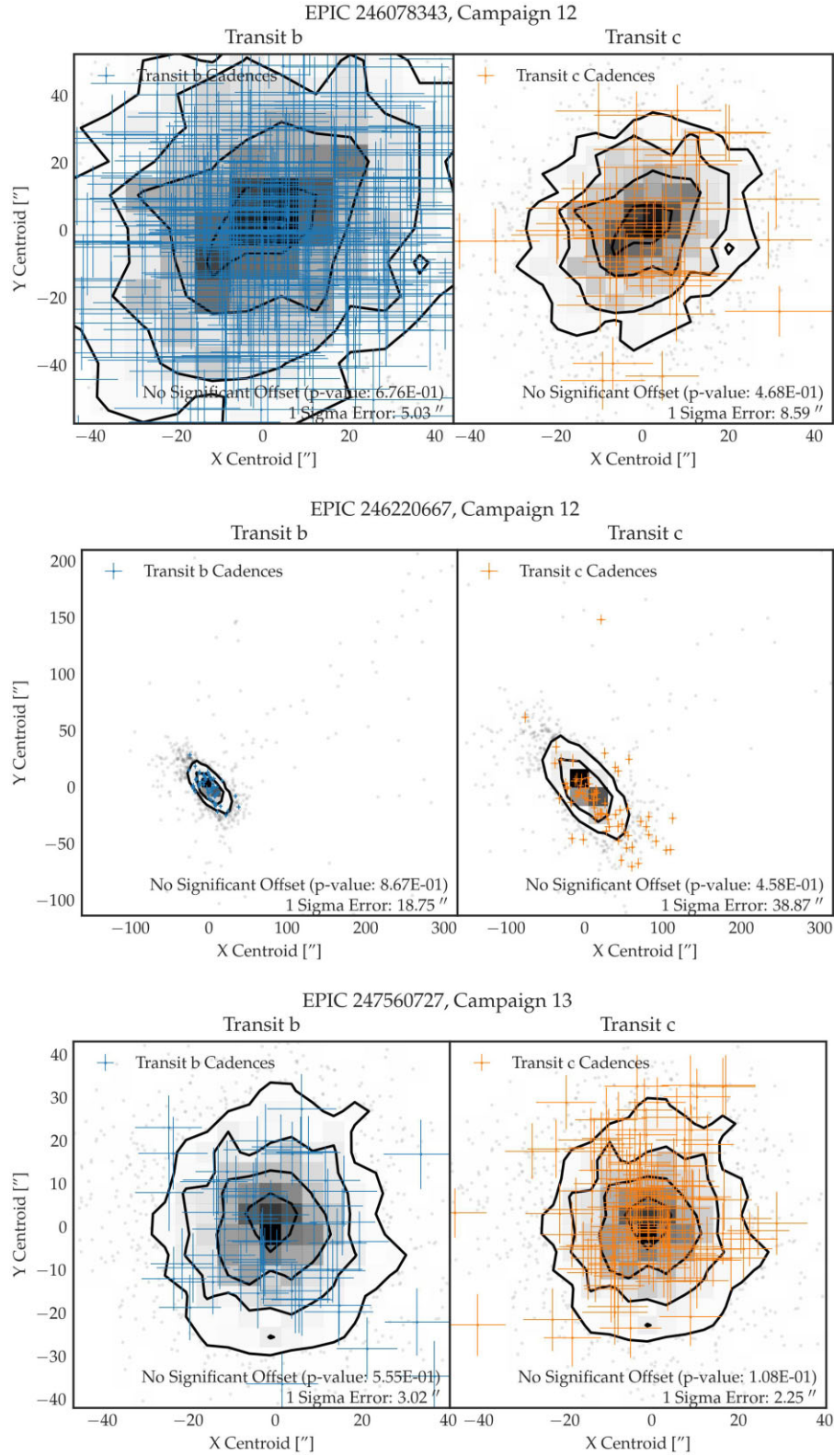
Figure 9. Centroid plots for all multiplanetary candidates listed in Table 3. The in-transit cadences centroid locations are denoted in blue while the out-of-transit centroid locations are denoted in grey. The 1σ, 2σ, and 3σ contours of the centroids of the out-of-transit cadences are also represented.
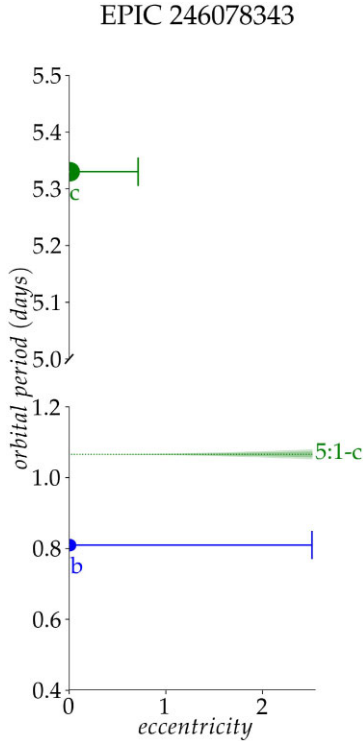
EPIC 246078343

EPIC 246220667

Figure 10. Resonance locations in the K2-413 system. The horizontal axis denotes the eccentricity while the vertical axis shows the orbital period (note that the *y*-axis is discontinuous and not to scale). The location of the planets K2-413 b and K2-413 c are represented in blue and green circles, respectively, and the solid horizontal lines extend to the eccentricity at which each planet would cross the next planet's orbit. The orbital periods for these two planets are too separated to obtain resonant orbits.

4.4 Highlights of our planet candidate sample

4.4.1 *EPIC 247560727.01 and EPIC 247560727.02*

EPIC 247560727 is a faint ($K_{\rm p}$ = 15.164 mag, G = 15.442 mag, J = 13.577 mag) G8 star ($0.779^{+0.059}_{-0.054}\,R_{\odot}$, $0.693^{+0.301}_{-0.212}\,M_{\odot}$; Hardegree-Ullman et al. 2020) observed during *K2* campaign C13. It is located at (α, δ) = (05:01:42.22, 22:39:41.81) at a distance of ~681 pc (Bailer-Jones et al. 2021). It is a multiplanetary candidate system consisting of two planets with periods 3.3733 ± 0.0002 and $8.4356^{+0.0001}_{-0.0006}$ d. The `vespa` and `TRICERATOPS` FPP values are 10^{-3} and 0.013 for EPIC 247560727.01, and 0.03 and 0.028 for EPIC 247560727.01. We do not validate this system due to the presence of a nearby, slightly fainter (G = 16.584 mag) star at ~3 arcsec from EPIC 247560727. Given that this distance is of the order of the *Kepler* pixel size, we can not differentiate the host star using the *K2* photometry alone. Table 6 shows a comparison of the stellar properties for EPIC 247560727 and the neighbouring star TIC 674662900. The latter seems to be a background star not bound to EPIC 247560727 given the differences in the proper motions and the parallaxes obtained from *Gaia* eDR3. In addition, the astrometric information from *Gaia* eDR3 (i.e. GOF_AL, D, and RUWE) for both targets initially rules out the possibility of both stars being binaries on their own. The centroid computed distances to the nearest neighbouring star (see the last row of Fig. 9) also cannot discard the possibility of TIC 674662900 being the host star, though the 2.25 arcsec distance for EPIC 247560727.02 seems to favour the brightest star as the transiting one. Assuming that EPIC 247560727 is the host star of these planet candidates,
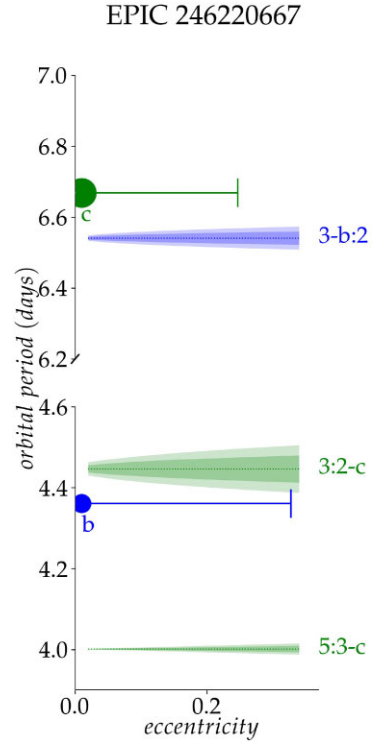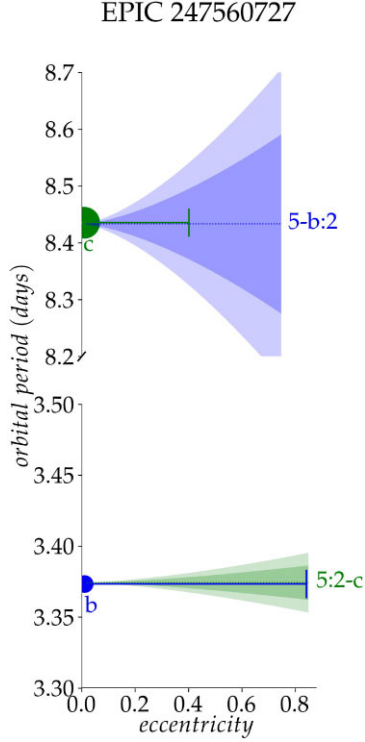
Figure 11. Resonance locations in the K2-414 system. Same notation as Fig. 10. The dashed lines show the location of the estimated 3:2 and 5:3 mean motion resonances for planets K2-414 b and K2-414 c. The shaded regions around each resonance are the widths corresponding to the lower (dark shading) and upper (light shading) planet mass limits, propagated from the radii uncertainties, and estimated using the *Kepler* mass-radius relationship from Kanodia et al. (2019). The label '5:3-c' indicates that a test particle at that location would complete three orbits in the same amount of time that planet c takes to complete five orbits.

EPIC 247560727.01 is a super-Earth ($1.5838 \pm 0.0781\,R_{\oplus}$) orbiting at a distance of $0.0279^{+0.0013}_{-0.0016}$ au and EPIC 247560727.02 is a sub-Neptune ($2.9192^{+0.4080}_{-0.3350}\,R_{\oplus}$) orbiting at a distance of $0.0708^{+0.0051}_{-0.0056}$ au. Using the *Kepler* mass-radius relationship from Kanodia et al. (2019), we estimate planetary masses of ~4.24 and ~6.78 $M_{\oplus}$. Using these planetary masses, the detected periods and the resonance analysis explained in Section 3.7, we find that both planets are in a 5:2 resonant orbit (see Fig. 12), similar to the Jupiter and the Saturn in the Solar system. This fact suggests that both planet candidates are orbiting the same star rather than each one of them orbiting a different host star. Using the dilution factor (see Section 3.4) and assuming that the depths in the *Gaia* bandpass are of the same order as in the *Kepler* one (both filters are centred approximately at the same wavelength, and have similar bandwidths), the planetary radii would be a factor ~1.16 × larger if the planets are orbiting EPIC 247560727 and ~1.96 × larger if the host star is TIC 674662900. This would still put both candidates well below the $R_{\rm p} < 8\,R_{\oplus}$ brown-dwarf/stellar limit.

4.4.2 *EPIC 211436876.01*

EPIC 211436876 is a relatively bright ($K_{\rm p}$ = 12.302 mag, G = 12.279 mag, J = 11.335 mag) G2 star ($1.057^{+0.022}_{-0.020}\,R_{\odot}$, $0.992^{+0.068}_{-0.063}\,M_{\odot}$; Hardegree-Ullman et al. 2020) observed by *K2* during campaigns C5 and C18. It is located at (α, δ) = (08:30:54.63, 12:11:56.77) at a distance of ~370 pc (Bailer-Jones et al. 2021).

Table 6. Comparison of stellar properties for EPIC 247560727 and contaminating background star TIC 67462900.

EPIC	TIC	$R_\odot$	$M_\odot$	$T_{\rm eff}$	$\log g$	GOF_AL	D	RUWE	pm [mas yr^{-1}]	Π [mas]
27560727	69054629	$0.779^{+0.059}_{-0.054}$	$0.693^{+0.301}_{-0.212}$	5634 ± 138	$4.494^{+0.150}_{-0.150}$	-0.83	0.0	0.96	4.92	1.431
–	674662900	$1.288^{\dagger}$	$1.210^{\dagger}$	$6252 \pm 128^{\dagger}$	$4.301^{\dagger}$	-1.24	0.0	0.94	1.90	0.338

Note. †: data from TIC catalogue (Paegert et al. 2021).

Figure 12. Resonance locations in the EPIC 247560727 system. Same notation as Fig. 10. The dashed lines show the location of the estimated 5:2 mean motion resonance for planets EPIC 247560727.01 and EPIC 247560727.02. The shaded regions around each resonance are the widths corresponding to the lower (dark shading) and upper (light shading) planet mass limits, propagated from the radii uncertainties and estimated using the *Kepler* mass-radius relationship from Kanodia et al. (2019). Both planet candidates are in a 5:2 resonance, similar to the Jupiter and the Saturn in the Solar system.

We detect a significant period of $1.1524^{+0.0003}_{-0.0004}$ d in the EVEREST 2.0 and TFAW light curves for both sectors (and in the combined C5 + C18 light curves), and a harmonic of the period in the K2SFF light curves (although they have $\sim$1.6 $\times$ worse photometric precision than the EVEREST 2.0 ones). EPIC 211436876.01 is a candidate sub-Earth ($0.6746^{+0.0454}_{-0.0392} R_\oplus$) orbiting at a distance of $0.0125^{+0.0009}_{-0.0011}$ au and receiving a stellar insolation of $\sim$8270 $S/S_\oplus$. The vespa and TRICERATOPS FPP values for this target are 0.4624 and 0.1054, respectively. The centroid p-value is 0.405 and the maximum computed separation for a background eclipsing binary is 612.23 arcsec (see Fig. 8). There are two nearby ($\sim$15.5 and $\sim$18 arcsec) fainter ($G = 17.983$ and 16.591 mag) stars partially affecting the EVEREST 2.0 aperture. Following our vetting procedure (see Section 3.2), we recomputed the light curves for both campaigns, changing the aperture size in order to minimize the flux contribution from these neighbouring stars. Also, we could not recover the transiting signal when creating custom apertures centred in the neighbouring stars using the lightkurve pipeline.

The *Gaia* astrometric parameters (see Table 7) for these two stars seem to rule-out the chances of them being background binary stars. Using the mass-radius estimation from Chen & Kipping (2016), we compute an estimated mass of $\sim$0.24 $M_\oplus$, this results in a very small RV semi-amplitude of $K \sim 0.15 \, {\rm m \, s^{-1}}$. Also, although orbiting a relatively bright star, the photometric follow-up of this target is challenging given the small transit depth ($<$0.1 ppt). However, if confirmed, it would be one of the few very short-period ($<$1.5 d) sub-Earths (with $R_{\rm p} < 0.7 \, R_\oplus$) to be detected (LHS 1678 b (Silverstein et al. 2022); Kepler-1351 b, and Kepler-1087 b (Morton et al. 2016)), the second in the *K2* mission (after K2-89 b (Crossfield et al. 2016)), and also, the second around a G-type star (after Kepler-1087 b).

4.4.3 EPIC 210706310.01

EPIC 210706310 is a relatively bright ($K_{\rm p} = 12.294$ mag, $G = 12.296$ mag, $J = 11.083$ mag), metal-poor ([Fe/H] $= -0.402 \pm 0.235$ [dex], Hardegree-Ullman et al. (2020); [Fe/H] $= -0.463428^{+0.35536}_{-0.230723}$ [dex], Anders et al. (2022); [Fe/H] $= -0.252370 \pm 0.081465$ [dex], Buder et al. (2021)), F7 star ($0.954^{+0.055}_{-0.052} R_\odot$, $0.709^{+0.304}_{-0.219} M_\odot$) (Hardegree-Ullman et al. 2020) observed by *K2* in campaign C4. It is located at $(\alpha, \delta) = $ (03:57:30.02, 18:27:13.13) at a distance of $\sim$275 pc (Bailer-Jones et al. 2021). We detect a significant period of 5.1718 ± 0.0002 d in the *K2* pipeline, EVEREST 2.0, and K2SFF light curves. EPIC 210706310.01 is a candidate sub-Earth ($0.8891^{+0.0529}_{-0.0443} R_\oplus$) orbiting at a distance of $0.0510^{+0.0024}_{-0.0029}$ au, and receiving a stellar insolation of $\sim$391 $S/S_\oplus$. Even though its vespa FPP is below the 1 per cent threshold, we do not validate this target due to the presence of a very faint ($G = 20.247$ mag) background star at a distance of $\sim$6.4 arcsec. Also, the TRICERATOPS results point as the most probable scenarios either the transiting planet around the target (57 per cent), the unresolved bound companion with the transiting planet around the primary star (16 per cent) or the secondary star (22 per cent). The *Gaia* eDR3 astrometric parameters (GOF_AL = 1.32, D = 7.07, RUWE = 1.052) seem to disfavour the binary scenario for this target. Also, the astrometric values (GOF_AL = $-$1.23, D = 1.27×10^{-15}, RUWE = 0.944) for the faint background star seem to discard it from being a background eclipsing binary. Data from future *Gaia* releases might help to improve the characterization of this system. Candidates orbiting metal-poor stars like this one can help planet formation theories by setting limits to the lowest metallicity that protoplanetary discs can have to form planets (Matsuo et al. 2007; Gáspár, Rieke & Ballering 2016; Petigura et al. 2018).

4.5 False positives

Out of our sample of 27 planetary candidates, 8 of them have either not passed the vetting procedure in Section 3.2 or have FPPs exceeding the thresholds defined in Section 3.6. EPIC 220356827.01 (with FPP$_{\rm TRICERATOPS}$ = 0.4558 and FPP$_{\rm vespa}$ = 0.9834), and

Table 7. Comparison of *Gaia* properties for EPIC 211436876 and nearby stars.

EPIC	*Gaia* eDR3	*G* [mag]	GOF_AL	D	RUWE
211436876	602703487815096832	12.28	− 2.72	2.36	0.88
211437101	602703487814896384	17.98	1.07	0.70	1.04
211436674	602702731900653568	16.59	0.39	0.00	1.02
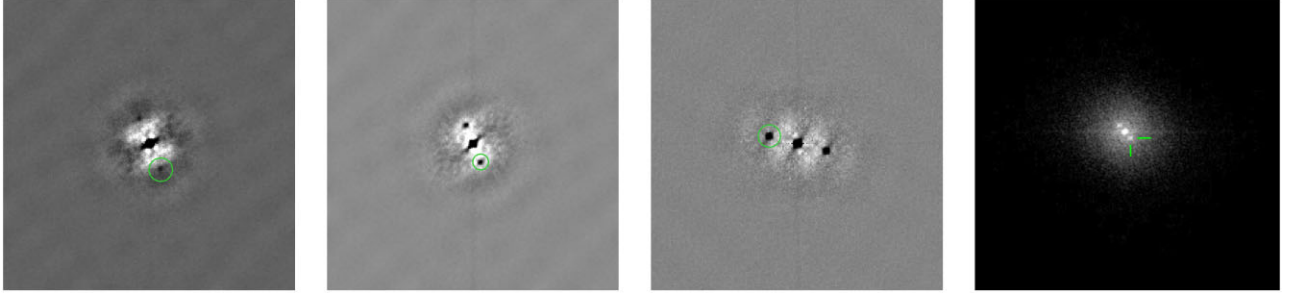
Figure 13. SOAR speckle auto-correlations for EPIC 205979843 (left), EPIC 246022853 (middle left), and EPIC 246163416 (middle right) with detected nearby companions marked in green. The field size is 3.15 arcsec, north-up and east-left. BTA observations for EPIC 211572480 (right) with the detected companion marked in green, north-up and east-left.

EPIC 246048459.01 (with FPP$_{\mathrm{TRICERATOPS}}$ = 0.9836 and FPP$_{\mathrm{vespa}}$ = 0.3407) have failed the validation process. In the case of the former, the transit shape is v-shaped and different during the egress. In addition, there is some excess flux during the ingress that could point towards a binary nature of the system. In the case of the latter, although the *Gaia* astrometric parameters and the SOAR speckle imaging seem to rule out the presence of contaminating stars, the FPP values make us mark this candidate as a false positive.

4.5.1 False positives by Gaia *eDR3*

Of the remaining six false positives systems, five of them (EPIC 211572480, EPIC 211705502, EPIC 220471100, EPIC 246022853, and EPIC 246163416) have been discarded following the criteria in Section 2.5 for *Gaia* eDR3 GOF_AL, D, and RUWE values. EPIC 211572480 and EPIC 211705502 have missing stellar properties both from the EPIC catalogue (Huber et al. 2017) and from Hardegree-Ullman et al. (2020) data. EPIC 211572480 has very large GOF_AL, D, and RUWE values (see Table 2) that point towards the binary nature of the system. We detect a companion at ∼0.1 arcsec and Δ mag ∼ 0 using BTA speckle imaging using the 550/50 filter (see Fig. 13). EPIC 211705502 was first reported to have a transiting object of R_{p} = 10.29 $R_{\oplus}$ in a P = 2.58 d orbit by Castro-González et al. (2021). They used *isochrones*-derived stellar parameters to derive the planetary parameters, they took into account the presence of two fainter and nearby stars (separated ∼1.17 and ∼5.88 arcsec), and with *Gaia* DR2 GOF_AL = 0.57 and D = 0.00, FPP$_{\mathrm{vespa}}$ = 0.99 values, they catalogued EPIC 211705502.01 as a candidate transiting exoplanet. Using updated *Gaia* eDR3 data (GOF_AL = 30.94, D = 57.8, and RUWE = 2.42), we denote this candidate as a false positive. The two other nearby stars with GOF_AL = 3.87, D = 4.54, and GOF_AL = 0.83, D = 0.48, and RUWE = 1.031, respectively, do not seem to be the source of the transiting signal. Given the low-SNR BTA observations for this target, we could not obtain conclusive results for the presence of companions. EPIC 246022853 and EPIC

246163416 have resolved companions from SOAR speckle imaging data (see Fig. 13 and Table 8), as well as large values for the *Gaia* parameters. Except for the case of EPIC 220471100, where we do not detect any companion star using BTA, there seems to be a good agreement between speckle imaging and *Gaia* eDR3 astrometric parameters. These seem to confirm that the use of these parameters could be a good way of determining probable false positive scenarios during the vetting stage of future planet candidates.

The remaining false positive system, EPIC 205979483, has a very faint (ΔI = 4 mag) companion detected through SOAR speckle imaging at a distance of 0.5751 arcsec (see Fig. 13). Interestingly, both D = 15.1 and RUWE = 1.41 exceed the threshold values defined in Section 2.5, and although the GOF_AL = 7.19 is smaller than the defined limit, it is the highest value of all the systems that have passed these vetting criteria. This result seems to indicate that caution has to be taken for planetary candidates whose *Gaia* parameters are close to the theoretical values, and also, reinforces the fact that high-resolution imaging through speckle and/or adaptive optics are needed in order to better characterize these systems. Regarding this, one consideration has to be done for our planet candidate EPIC 210967369.01. Even though it has a slightly large RUWE value of 1.28, a slightly smaller value of GOF_AL (5.44) than EPIC 205979483, and relatively large FPP values (FPP$_{\mathrm{vespa}}$ = 0.8165 and FPP$_{\mathrm{TRICERATOPS}}$ = 0.266) due to the presence of a nearby (∼19.7 arcsec), fainter (*G* = 19.727) background star, we classify it as a planet candidate; but taking into consideration that it might benefit from new astrometric values from future *Gaia* data releases.

In the case of EPIC 246163416, we detect a slightly fainter (ΔI = 0.7 mag) companion at a distance of 0.6289 arcsec (see Fig. 13) through SOAR speckle imaging. The *Gaia* eDR3 parameters for this target (see Table 2) point towards the binary nature of the system. However, the angular separation of the SOAR companion is not compatible with the detected transiting period of P = 0.8768 d. Thus, a third object is present as either part of a trinary system (more observations would be needed in order to determine whether the
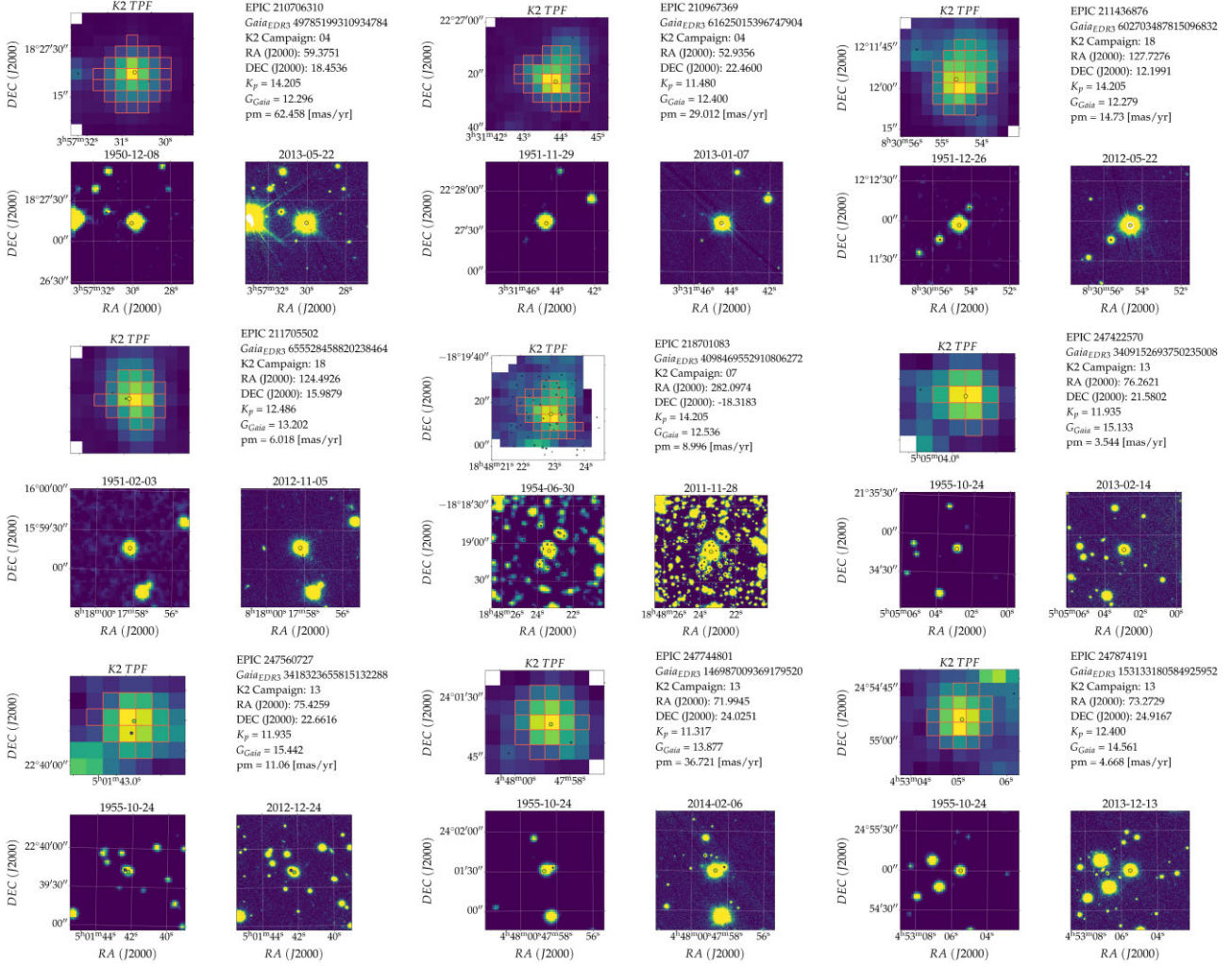
Figure 14. Seeing limited imaging validation sheets for those targets in our sample with detected *Gaia* eDR3 companions within the `EVEREST 2.0` photometric aperture. In each validation sheet, *top left*: *K2* target pixel file (TPF) with the `EVEREST 2.0` aperture (red squares) superposed. *Lower left*: Palomar Observatory Sky Survey (POSS-I) images. *Lower right*: Pan-STARRS DR2 images. *Gaia* eDR3 sources are represented with coloured points.

Table 8. Systems with detected companions in SOAR speckle imaging data (2021.75–2021.80).

EPIC	ρ [arcsec]	Θ [°]	ΔI [mag]
205979483	0.5751	203.2	4.0
246022853	0.4305	201.2	2.7
246163416	0.6289	75.9	0.7
211572480	0.1000	225.0	0.1

SOAR companion is gravitationally bound to the EPIC target) or transiting one of the stars in a binary configuration. The MCMC best-fitting planetary radius ($R_{\rm p} = 8.4683^{+4.3149}_{-2.8121}\,R_{\oplus}$), and the retrograde and high-orbit inclination angle ($i = 140.52°^{+2.2073}_{-2.1373}$) seem to point towards a grazing binary scenario as the most probable one for this candidate.

5 CONCLUSIONS

The *K2* sub-Neptune-sized planetary legacy is a niche that still remains to be fully exploited. Algorithms able to increase the

photometric precision of the *K2* light curves can help increase the number of detected exoplanets orbiting fainter stars or of different spectral types. In this sense, `TFAW` denoising together with `TLS` improved detection capabilities offer a new way of detecting and characterizing planetary transit candidates missed by previous works. In this work, we have presented the results from a first sample of 27 planetary candidates from the `TFAW` survey. Combining `vespa` and `TRICERATOPS` FPPs, we statistically validate six planets in four different stellar systems and present 12 planetary candidates, of which 11 are new detections. Our sample of validated and candidate planets is comprised of three sub-Earth planets, seven Earth-sized planets, four super-Earths, and four sub-Neptunes. With respect to individual systems, we highlight the following: a validated highly-irradiated Earth-sized planet (K2-411 b), and a validated sub-Neptune planet (K2-412 b) orbiting a G4 star. Two validated multiplanetary systems, K2-413 and K2-414; the latter near its 3:2 mean motion resonance. A candidate multiplanetary system EPIC 247560727 consists of a super-Earth and sub-Neptune in a 5:2 resonant orbit. And EPIC 21436876.01 is a very-short period sub-Earth candidate, and one of the few detected orbiting around a G2 star. In addition, one of our validated planets and one candidate are

USP planets. Given their estimated escape velocities and effective temperatures, four of our planet candidates and one validated planet are close to the He atmospheric escape threshold and within the Radius Gap. With its estimated density, candidate planet EPIC 247560727.02 would probably be a water world. Although affected by the presence of contaminating background stars, planet candidate EPIC 218701083.01 could be one of the few planets within the Neptunian Desert. Given the improvements obtained with TFAW, eight listed planets have radii below the Radius Gap. Finally, we classify eight candidates as false positives. We find from combining speckle imaging and *Gaia* eDR3 photometric and astrometric information that *Gaia* data can be a powerful tool that can benefit the vetting process of future planet candidates.

By increasing the number of statistically validated and candidate planets, TFAW aims to expand the statistical information of the population of planets. This can have an impact on improving the planet occurrence rates, affect the current and future planet formation and evolution theories and their role on habitability conditions, and improve our understanding of star-planet interactions, atmospheric erosion, and other phenomena.

DATA AVAILABILITY

The data presented in this article will be shared on reasonable request to the corresponding author.

REFERENCES

Adams E. R., Jackson B., Endl M., 2016, AJ, 152, 47
Adams E. R. et al., 2021, PSJ, 2, 152
Anders F. et al., 2022, A&A, 658, A91
Armstrong D. J., Gamper J., Damoulas T., 2021, MNRAS, 504, 5327
Bailer-Jones C. A. L., Rybizki J., Fouesneau M., Demleitner M., Andrae R., 2021, AJ, 161, 147
Balega I. I., Balega Y. Y., Hofmann K. H., Maksimov A. F., Pluzhnik E. A., Schertl D., Shkhagosheva Z. U., Weigelt G., 2002, A&A, 385, 87
Barros S. C. C., Demangeon O., Deleuil M., 2016, A&A, 594, A100
Batalha N. M. et al., 2010, ApJ, 713, L103
Bernardo J., Berger J. O., Dawid A. P., Smith A. F. M., 1996, Proc. Fifth Valencia International Meeting, Bayesian Statistics 5. Clarendon Press, Oxford
Borucki W. J. et al., 2011, ApJ, 736, 19
Bryson S. T. et al., 2013, PASP, 125, 889
Buder S. et al., 2021, MNRAS, 506, 150
Castro González A. et al., 2020, MNRAS, 499, 5416
Castro-González A. et al., 2021, MNRAS, 509, 1075
Chen J., Kipping D., 2016, ApJ, 834, 17
Chen D.-C. et al., 2022, AJ, 163, 249
Christiansen J. L. et al., 2022, AJ, 163, 244
Claret A., 2018, A&A, 618, A20
Clark C. A., van Belle G. T., Horch E. P., Trilling D. E., Hartman Z. D., Collins M., von Braun K., Gehring J., 2020, in Tuthill P. G., Mérand A., Sallum S., eds, Proc. SPIE Cof. Ser. Vol. 11446, Optical and Infrared Interferometry and Imaging VII. SPIE, Bellingham, p. 114462A
Crossfield I. J. M. et al., 2016, ApJS, 226, 7
Crossfield I. J. M. et al., 2018, ApJS, 239, 5
Cui X.-Q. et al., 2012, Res. Astron. Astrophys., 12, 1197
Daemgen S., Hormuth F., Brandner W., Bergfors C., Janson M., Hippler S., Henning T., 2009, A&A, 498, 567
Dattilo A. et al., 2019, AJ, 157, 169
de Leon J. P. et al., 2021, MNRAS, 508, 195
del Alcázar M., del Ser D., Fors O., 2021, TFAW K2 Survey: an Insight into a few Hundreds of New Earth-Sized Planetary Candidates. CS20.5, Cambridge Workshop on Cool Stars, Stellar Systems, and the Sun. Zenodo, available at https://doi.org/10.5281/zenodo.4549022
del Ser D., Fors O., 2020, MNRAS, 498, 2778
del Ser D., Fors O., Núñez J., 2018, A&A, 619, A86
Deming D. et al., 2015, ApJ, 805, 132
Díaz R. F., Almenara J. M., Santerne A., Moutou C., Lethuillier A., Deleuil M., 2014, MNRAS, 441, 983
Evans D. F., 2018, RNAAS, 2, 20
Evans D. F., Southworth J., Smalley B., 2016, ApJ, 833, L19
Flewelling H. A. et al., 2020, ApJS, 251, 7
Foreman-Mackey D., 2018, RNAAS, 2, 31
Foreman-Mackey D., Hogg D. W., Lang D., Goodman J., 2013, PASP, 125, 306
Foreman-Mackey D., Agol E., Ambikasaran S., Angus R., 2017, AJ, 154, 220
Foreman-Mackey D. et al., 2021, J. Open Source Softw., 6, 3285
Fulton B. J. et al., 2017, AJ, 154, 109
Gaia Collaboration, 2021, A&A, 649, A1
Gandhi P. et al., 2022, MNRAS, 510, 3885
Gáspár A., Rieke G. H., Ballering N., 2016, ApJ, 826, 171
Giacalone S., Dressing C. D., 2020, triceratops: Candidate Exoplanet Rating Tool. Astrophysics Source Code Library, record ascl:2002.004
Giacalone S. et al., 2021, AJ, 161, 24
Gillon M. et al., 2017, Nature, 542, 456
Ginzburg S., Schlichting H. E., Sari R., 2018, MNRAS, 476, 759
Hamer J. H., Schlaufman K. C., 2020, AJ, 160, 138
Hardegree-Ullman K. K., Zink J. K., Christiansen J. L., Dressing C. D., Ciardi D. R., Schlieder J. E., 2020, ApJS, 247, 28
Hedges C., 2021, RNAAS, 5, 262
Heller R., Hippke M., Rodenbeck K., 2019, A&A, 627, A66
Hippke M., Heller R., 2019, A&A, 623, A39
Hirano T. et al., 2018, AJ, 155, 127
Horch E. P., van Belle G. T., Davidson, James W. J., Ciastko L. A., Everett M. E., Bjorkman K. S., 2015, AJ, 150, 151
Howell S. B. et al., 2014, PASP, 126, 398
Huber D., Bryson S. T. et al., 2017, VizieR Online Data Catalog, IV/34
Kanodia S., Wolfgang A., Stefansson G. K., Ning B., Mahadevan S., 2019, ApJ, 882, 38
Kasting J. F., 1988, Icarus, 74, 472
Kipping D. M., 2013, MNRAS, 435, 2152
Kipping D. M., 2014, MNRAS, 440, 2164
Kopparapu R. K. et al., 2013, ApJ, 765, 131
Kovacs G., 2020, A&A, 643, A169
Kovács G., Zucker S., Mazeh T., 2002, A&A, 391, 369
Kovács G., Zucker S., Mazeh T., 2005, MNRAS, 356, 557
Kruse E., Agol E., Luger R., Foreman-Mackey D., 2019, ApJS, 244, 11

Lam K. W. F. et al., 2021, Science, 374, 1271

Lightkurve Collaboration, 2018, Lightkurve: Kepler and TESS time series analysis in Python. Astrophysics Source Code Library, record ascl:1812.013

Lissauer J. J. et al., 2011, ApJS, 197, 8

Lissauer J. J. et al., 2011, Nature, 470, 53

Lissauer J. J. et al., 2012, ApJ, 750, 112

Lissauer J. J. et al., 2014, ApJ, 784, 44

Livingston J. H. et al., 2018, AJ, 156, 277

Luger R., Kruse E., Foreman-Mackey D., Agol E., Saunders N., 2018, AJ, 156, 99

Lund M. N., Handberg R., Davies G. R., Chaplin W. J., Jones C. D., 2015, ApJ, 806, 30

Lundkvist M. S. et al., 2016, Nat. Commun., 7, 11201

Maksimov A. F., Balega Y. Y., Dyachenko V. V., Malogolovets E. V., Rastegaev D. A., Semernikov E. A., 2009, Astrophys. Bull., 64, 296

Matsuo T., Shibai H., Ootsubo T., Tamura M., 2007, ApJ, 662, 1282

Mayo A. W. et al., 2018, AJ, 155, 136

McDonald G. D., Kreidberg L., Lopez E., 2019, ApJ, 876, 22

Mitrofanova A., Dyachenko V., Beskakotov A., Balega Y., Maksimov A., Rastegaev D., Komarinsky S., 2020, AJ, 159, 266

Morton T. D., 2012, ApJ, 761, 6

Morton T. D., 2015a, VESPA: False positive probabilities calculator. Astrophysics Source Code Library, record ascl:1503.011

Morton T. D., 2015b, isochrones: Stellar Model Grid Package. Astrophysics Source Code Library,record ascl:1503.010

Morton T. D., Bryson S. T., Coughlin J. L., Rowe J. F., Ravichandran G., Petigura E. A., Haas M. R., Batalha N. M., 2016, ApJ, 822, 86

Ning B., Wolfgang A., Ghosh S., 2018, ApJ, 869, 5

Owen J. E., Wu Y., 2013, ApJ, 775, 105

Owen J. E., Wu Y., 2017, ApJ, 847, 29

Paegert M., Stassun K. G., Collins K. A., Pepper J., Torres G., Jenkins J., Twicken J. D., Latham D. W., 2021, preprint (arXiv:2108.04778)

Penoyre Z., Belokurov V., Evans N. W., 2022, MNRAS, 513, 5270

Pepe F. A. et al., 2010, in McLean I. S., Ramsay S. K., Takami H., eds, Proc. SPIE Conf. Ser. Vol. 7735, Ground-based and Airborne Instrumentation for Astronomy III. SPIE, Bellingham, p. 77350F

Petigura E. A., 2020, AJ, 160, 89

Petigura E. A. et al., 2018, AJ, 155, 89

Petigura E. A. et al., 2022, AJ, 163, 179

Pluzhnik E. A., 2005, A&A, 431, 587

Quirrenbach A. et al., 2010, in McLean I. S., Ramsay S. K., Takami H., eds, Proc. SPIE Conf. Ser. Vol. 7735, Ground-based and Airborne Instrumentation for Astronomy III. SPIE, Bellingham, p. 773513

Ribas I., Guinan E. F., Güdel M., Audard M., 2005, ApJ, 622, 680

Salvatier J., Wiecki T. V., Fonnesbeck C., 2016, PeerJ Comput. Sci., 2, e55

Sanchis-Ojeda R., Rappaport S., Winn J. N., Kotson M. C., Levine A., Mellah I. E., 2014, ApJ, 787, 47

Silverstein M. L. et al., 2022, AJ, 163, 151

Skrutskie M. F. et al., 2006, AJ, 131, 1163

Tokovinin A., 2018, PASP, 130, 035002

Torres G. et al., 2015, ApJ, 800, 99

Uzsoy A. S. M., Rogers L. A., Price E. M., 2021, ApJ, 919, 26

Vanderburg A., Johnson J. A., 2014, PASP, 126, 948

Vanderburg A. et al., 2016, ApJS, 222, 14

Venturini J., Helled R., 2017, ApJ, 848, 95

West R. G. et al., 2019, MNRAS, 486, 5094

Winn J. N., Sanchis-Ojeda R., Rappaport S., 2018, New Astron. Rev., 83, 37

Zeng L., Jacobsen S. B., Sasselov D. D., 2017, RNAAS, 1, 32

Zeng L. et al., 2019, Proc. Natl. Acad. Sci., 116, 9723

Zink J. K., Hardegree-Ullman K. K., Christiansen J. L., Dressing C. D., Crossfield I. J. M., Petigura E. A., Schlieder J. E., Ciardi D. R., 2020, AJ, 159, 154

Zink J. K. et al., 2021, AJ, 162, 259

Zsom A., Seager S., de Wit J., Stamenković V., 2013, ApJ, 778, 109

This paper has been typeset from a T$_E$X/L^{A}T$_E$X file prepared by the author.